From Groundwork to Efficient Solar Cells: On the Importance of the Substrate Material in Co-Evaporated Perovskite Solar Cells

Tobias Abzieher,* Thomas Feeney, Fabian Schackmar, Yidenekachew J. Donie, Ihteaz M. Hossain, Jonas A. Schwenzer, Tim Hellmann, Thomas Mayer, Michael Powalla, and Ulrich W. Paetzold*

Vacuum-based deposition of optoelectronic thin films has a long-standing history. However, in the field of perovskite-based photovoltaics, these techniques are still not as advanced as their solution-based counterparts. Although high-efficiency vacuum-based perovskite solar cells reaching power conversion efficiencies (PCEs) above 20% are reported, the number of studies on the underlying physical and chemical mechanism of the co-evaporation of lead iodide and methylammonium iodide is low. In this study, the impact of one of the most crucial process parameters in vacuum processes—the substrate material—is studied. It is shown that not only the morphology of the co-evaporated perovskite thin films is significantly influenced by the surface polarity of the substrate material, but also the incorporation of the organic compound into the perovskite framework. Based on these studies, a selection guide for suitable substrate materials for efficient co-evaporated perovskite thin films is derived. This selection guide points out that the organic vacuum-processable hole transport material 2,2″,7,7″-tetra(N,N-di-p-tolyl)amino-9,9-spirobifluorene is an ideal candidate for the fabrication of efficient all-evaporated perovskite solar cells, demonstrating PCEs above 19%. Furthermore, building on the insights into the formation of the perovskite thin films on different substrate materials, a basic crystallization model for co-evaporated perovskite thin films is suggested.

1. Introduction

Without any doubts, metal-halide perovskite materials with the chemical composition ABX_3 have quickly evolved into one of the most outstanding material classes for optoelectronic applications in the early 21st century, covering a wide range of applications from light emitting devices such as light-emitting diode (LEDs) and light amplification by stimulated emission of radiation (LASERs) to light harvesting devices like optical sensors and solar cells.[1–3] Particularly in the field of photovoltaics (PV), where power conversion efficiencies (PCEs) exceeding 25% were demonstrated, perovskite-based solar cells have demonstrated tremendous progress within only one decade, already surpassing the record PCEs of much longer established technologies, namely simple multi-crystalline silicon, CdTe, and copper indium gallium diselenide (CIGS).[4,5]

Next to their beneficial optoelectronic properties such as high absorption coefficients,[6] long diffusion lengths,[7] and

Dr. T. Abzieher,[+] F. Schackmar, Y. D. Donie, Dr. J. A. Schwenzer, Prof. M. Powalla, Dr. U. W. Paetzold
Karlsruhe Institute of Technology (KIT)
Light Technology Institute (LTI)
Engesserstrasse 13, 76131 Karlsruhe, Germany
E-mail: tobias.abzieher@nrel.gov; ulrich.paetzold@kit.edu

T. Feeney, F. Schackmar, Y. D. Donie, Dr. I. M. Hossain, Dr. U. W. Paetzold
Karlsruhe Institute of Technology (KIT)
Institute of Microstructure Technology (IMT)
Hermann-von-Helmholtz-Platz 1, 76344 Eggenstein-Leopoldshafen, Germany

T. Hellmann, Dr. T. Mayer
Surface Science Laboratory, Materials Science Department
Technical University of Darmstadt
Alarich-Weiss-Strasse 2, 64287 Darmstadt, Germany

The ORCID identification number(s) for the author(s) of this article can be found under https://doi.org/10.1002/adfm.202104482.

[+]Present address: National Renewable Energy Laboratory (NREL), Golden, CO 80401, USA

**ADVANCED
SCIENCE NEWS**

www.advancedsciencenews.com

**ADVANCED
FUNCTIONAL
MATERIALS**

www.afm-journal.de

tunable bandgap,[8,9] the ease of fabricating high-quality thin films by a variety of techniques made them easily accessible and attractive for a large number of research groups. From a fabrication point of view, the current focus is clearly on solution-based deposition techniques, such as spin coating,[10–12] slot-die coating,[13–15] inkjet printing,[16–18] or spray coating[19–21] as they allow inexpensive integration in a laboratory environment as well as simple material and process optimization. Furthermore, these techniques promise an industrialized large-scale fabrication at low production costs.[22] Next to these solution-based deposition techniques, vacuum-based approaches have been suggested from early on as a promising route for the fabrication of high-quality perovskite thin films.[23,24] In fact, one of the first fabrications of a metal-halide perovskite material was performed by Mitzi et al. in a single-source evaporator in 1999, 10 years before the demonstration of its usability as a photovoltaic material by Kojima et al.[25,26] In 2015, co-evaporation was first introduced as an attractive deposition technique for lead chloride ($PbCl_2$) and methylammonium iodide (CH_3NH_3I, methylammonium iodide (MAI)) for the fabrication of efficient perovskite thin films in planar perovskite solar cells, allowing for non-stabilized PCEs as high as 15.4%.[27] However, already then the usual and seemingly simple monitoring of the co-evaporation process by quartz crystal monitors (QCMs) turned out to be challenging—primarily due to the high vapor pressure and low evaporation enthalpy of the organic compound. As an alternative to the monitoring of the film composition by rate detection, taking into account the omnidirectional evaporation of MAI, a combination of evaporation rate control of lead iodide (PbI_2) and pressure control of MAI was suggested by Teuscher et al. and employed by others.[28–30] However, PCEs demonstrated with this method lag behind results achieved with deposition processes monitored solely by QCMs. In addition, layer-by-layer deposition techniques have been introduced early on to avoid this problem.[31–33] In 2016, the performance of co-evaporated perovskite absorbers was further enhanced to PCEs as high as 20.3% by employing highly efficient organic charge transport layers, only slightly inferior to state-of-the-art solar cells prepared by solution-based techniques.[34] Moreover, this work pioneered the concept of fully vacuum-processed perovskite solar cells, which were further refined by employing organic and/or inorganic charge transport layers.[35–41]

Recent co-evaporation studies have advanced beyond the simple single-cation $CH_3NH_3PbI_3$ material to triple-cation,[42] methylammonium-free,[43–46] as well as lead-free and lead-reduced perovskite materials.[47–49] For solution-based perovskite solar cells, multi-cation and methylammonium-free perovskite materials have been reported to be a promising material system since they allow for easy bandgap tuning in addition to substantially better long-term stability.[50,51] The initial results demonstrated for co-evaporated materials are promising, however, remain lacking when compared with the high-efficiency multi-cation perovskite solar cells demonstrated for solution-based approaches.[10–12,50] Of particular interest for multi-junction solar cell applications,[52] where a wide-bandgap perovskite top solar cell is (monolithically) stacked on top of a low-bandgap perovskite,[53–55] silicon,[56–58] or CIGS bottom solar cell,[59,60] are optimized bandgaps that are larger than that of $CH_3NH_3PbI_3$. Recently, Longo et al. fabricated fully vacuum-processed

wide-bandgap perovskite solar cells with bandgaps of 1.72 eV and 1.87 eV with PCEs close to 16% by using a mixture of PbI_2 and lead bromide ($PbBr_2$) which are expected to be a promising material for multi-junction solar cells employing co-evaporated top solar cells.[61] Other vacuum-processed wide-bandgap materials have been introduced recently as well.[42,45,46] In addition, vacuum processing has been demonstrated to be capable to overcome the problem of inhomogeneous deposition on top of the textured and rough surfaces.[38,62–64] In that regard, Sahli et al. realized a fully texture two-terminal perovskite/silicon tandem solar cell with a PCE exceeding 25% by first evaporating PbI_2 on top of the textured silicon surface, followed by a solution-based conversion into perovskite.[58]

Despite the fact that promising results were obtained from vacuum-deposited perovskite absorbers and all-evaporated perovskite solar cells, thorough investigations into the co-evaporation process itself are rare. One of the selling points of vacuum processing is the significantly lower number of process parameters compared to solution-based techniques that are highly sensitive to the choice of solvents, process conditions, and even process atmosphere. In fact, the morphology and stoichiometry of a layer prepared in a perfect effusive vacuum process depend mostly on the evaporation rates of the individual materials, as well as the temperature and surface properties of the substrate material (i.e., the transparent conductive oxide and a charge transport layer the absorber is deposited on). Consequently, extreme care has to be taken when choosing the substrate material whereon the absorber is deposited. Preliminary studies on the interdependence of substrate material and electronic structure were performed for the co-evaporation of PbI_2 and MAI for a limited number of substrate materials.[65–68] In addition, thin-film formation for ultra-thin perovskite layers as well as for thin films based on $PbCl_2$ were studied.[69,70] Of particular note, metal oxide (e.g., titanium dioxide) substrate materials demonstrated only mediocre device performance but remarkable improvements were reported by adding a thin layer of an organic material between the metal oxide and the perovskite absorber.[40,62,68,71] In addition, significantly improved device performance was reported for deposition on top of nickel oxide hole transport layers, without the problems observed for other oxides.[37,38] While some studies indicate that organic charge transport layers are more suitable for the co-evaporation of perovskite absorbers,[34,40,62] a direct comparison between commonly employed substrate materials is lacking. However, for the future development of efficient vacuum-processed perovskite absorbers for single- and multi-junction devices, a clear guideline for the choice of substrate materials and an in-depth understanding of the nucleation and crystallization on different substrate materials is pivotal.

In response to this challenge, this work reports on the critical influence of commonly employed charge transport materials on the crystallization dynamics of co-evaporated perovskite thin films for use in solar cells. First, the fundamentals of the co-evaporation process of PbI_2 and MAI are recapitulated, illustrating that, as a result of the low enthalpy of evaporation of MAI, the co-evaporation process is best described by a mixture of an effusive process and a chemical vapor deposition (CVD) process, rather than a pure effusive process. The tremendous relevance of this insight is demonstrated by highlighting the

2104482 (2 of 19)

importance of the surface properties of the substrate material for the crystallization dynamics of co-evaporated perovskite thin films. Comparing perovskite thin films grown on different substrate materials, not only do morphology and crystallographic characteristics vary, but further the incorporation of MAI into the perovskite framework and, in turn, the composition of the thin film. Next, the fundamental processes during nucleation and crystallization of the co-evaporated thin films are investigated in detailed break-off experiments, allowing for additional insights about the influence of the substrate material, the development of a guideline for the choice of substrate material, as well as the postulation of a basic crystallization model for co-evaporated perovskite thin films. Finally, employing the proposed guidelines for the substrate material choice, the vacuum-processable organic hole transport material 2,2",7,7"-tetra(N,N-di-p-tolyl)amino-9,9-spirobifluorene (spiro-TTB) is shown to be an ideal candidate for the fabrication of high-quality co-evaporated perovskite absorbers for efficient all-evaporated perovskite solar cells.

2. Results

2.1. Recapitulating the Fundamentals of the Co-Evaporation Process for Hybrid Perovskites

Co-evaporation of PbI_2 and MAI was introduced early on as an effective deposition method of high-quality $CH_3NH_3PbI_3$ thin films for photovoltaic applications.[27] However, the exact nature of the co-evaporation process of PbI_2 and MAI and especially whether the deposition of MAI has to be considered and monitored as an effusive, a chemical-vapor-deposition-like, or a mixed process is still under extensive debate.[27,28,34,37,38,62,72,73] In this section, the underlying physical and chemical processes

that take place during co-evaporation of PbI_2 and MAI in the evaporation system used in this work are recapitulated from a conceptual point of view, as they form the basis for the following discussion on the influence on the substrate material on the perovskite thin-film formation in the herein employed deposition process. Similar to previous reports,[28–30,37,38] the co-evaporation process here is described to also have a CVD component in addition to the surface-mediated reactions on the substrate expected from a pure effusive deposition process. This change opens up additional chemical reaction paths at the surface of the substrate that are expected to significantly intensify the importance of the employed substrate material during co-evaporation. **Figure 1**a shows a schematic of the evaporation system employed in this study for co-evaporation of PbI_2 and MAI as well as the expected chemical reaction paths during the deposition between these two materials. In all reaction paths, evaporation of PbI_2 is considered to be a purely directed effusive process, which is legitimate considering the large mean free path of PbI_2 in the co-evaporation scenario (see discussion below).[74] In many previous works, deposition of MAI was controlled and monitored as if it were a purely effusive evaporating material, implying that both source materials are deposited simultaneously onto the substrate, controlled solely by the evaporation rates measured in close proximity to both individual evaporation sources. Kim et al. for example showed that a detection of MAI via QCMs can be employed if deposition and adhesion dynamics during co-evaporation are carefully modeled.[75] In their model it is considered that the reaction of PbI_2 and MAI into perovskite takes place at the substrate surface (see case 1 in Figure 1a) and a stoichiometric thin film is defined by the ratio of the individual evaporation rates of both source materials (while considering the complex adhesion properties during co-evaporation). However, contrary to this scenario, a two to
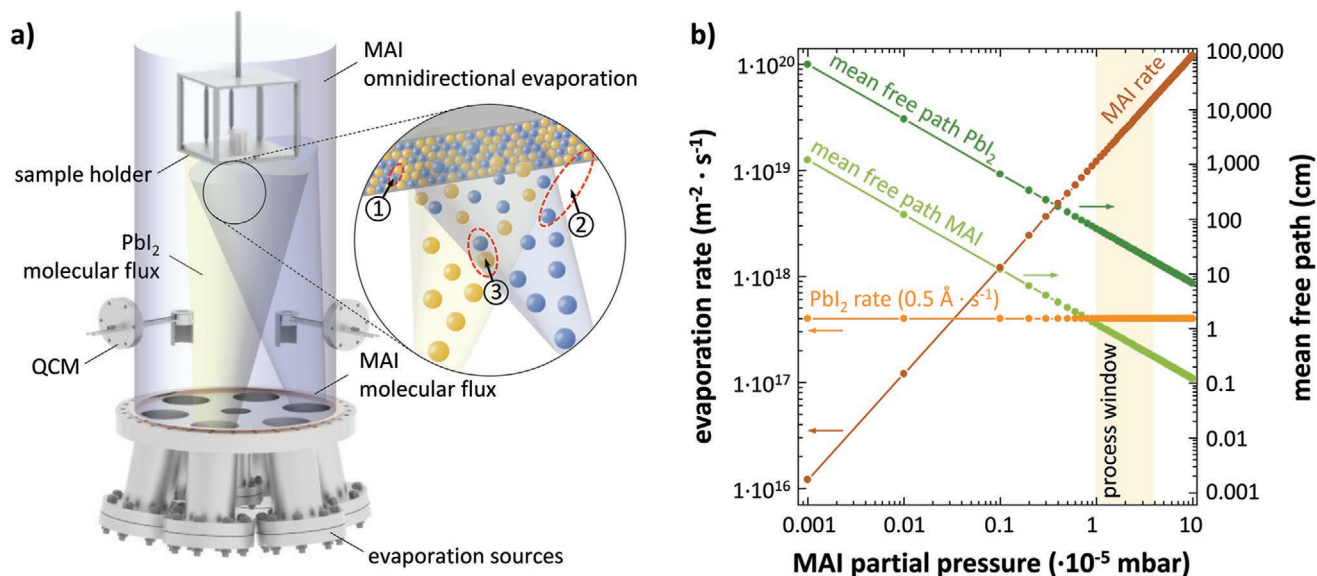
Figure 1. Schematic illustration of the employed evaporation system and chemical processes that can take place during the co-evaporation of PbI_2 and MAI. a) During co-evaporation three different reaction paths are conceivable: 1) a reaction of as-deposited PbI_2 and MAI on the substrate, 2) a delayed reaction of as-deposited PbI_2 with MAI from the environment, and 3) a reaction of PbI_2 and MAI before reaching the substrate. b) Theoretically expected evaporation rates and mean free paths of PbI_2 and MAI in an omnidirectional process atmosphere as a result of the high vapor pressure and low evaporation enthalpy of MAI.

three order of magnitude rise in background pressure (from ≈1 × 10^{-7} mbar to ≈5 × 10^{-5} mbar) as well as a deposition of MAI over time on parts of the vacuum system that cannot be due to a directed molecular flux (e.g., inside horizontal flanges facing away from the MAI source) is observed when MAI is heated above its evaporation point in the employed evaporation system in this study (see Figure S1, Supporting Information). The strong rise in background pressure is attributed to the comparatively high vapor pressure of MAI as a result of its low enthalpy of evaporation (see Figure S2, Supporting Information).[76] This is synonymous with a second undirected CVD component, that introduces major challenges to the co-evaporation process of perovskite-based thin films, and to the monitoring and adjustment of the thin film stoichiometry. Most importantly, the conversion of PbI$_2$ and MAI to perovskite in presence of a CVD component is not only limited to the simultaneous blending of both source materials on the substrate surface, as is the case of a purely effusive process, but additional conversion paths based on the direct interaction of PbI$_2$ with the MAI background pressure must be considered. In this regard, a pure PbI$_2$ film deposited on the substrate can be subsequently converted into perovskite via reaction with the MAI atmosphere around the substrate (see case 2 in Figure 1a) or in principle PbI$_2$ molecules can react with the MAI atmosphere to form perovskite on their path from evaporation source to substrate (see case 3 in Figure 1a). These considerations result in significant challenges in controlling and monitoring growth and composition during co-evaporation of metal-organic hybrid perovskite semiconductors.

The relevance of the co-existence of the individual reaction paths is illustrated by assessing the theoretical evaporation dynamics of co-evaporation in presence of a background CVD component. The evaporation rates of PbI$_2$ and MAI as well as their mean free paths in the background atmosphere formed during MAI evaporation for different partial pressures of MAI are calculated. In first approximation the evaporation rate (molecular flux) $j_{evaporation}$ is estimated by the Hertz–Knudsen equation (see Equation (1)):

$$j_{evaporation} = \frac{\alpha \cdot p}{\sqrt{2\pi m k_B T}} \tag{1}$$

where α is the sticking coefficient of molecules on the substrate, p the vapor pressure, m the mass of the molecule, k_B the Boltzmann constant, and T the temperature. In addition, the magnitude of mean free paths $\lambda_{molecule}$ for PbI$_2$ and MAI molecules moving through the MAI atmosphere with a partial pressure p_{MAI} is estimated based on the classical gas dynamics (see Equation (2)):

$$\lambda_{molecule} = \frac{4 k_B T}{\pi p_{MAI} \left(d_{molecule} + d_{MAI}\right)^2 \sqrt{\left(1 + \frac{M_{molecule}}{M_{MAI}}\right)}} \tag{2}$$

where d_{MAI} and $d_{molecule}$ are the respective diameters of the MAI molecule and the molecule that moves through the MAI atmosphere, while M_{MAI} and $M_{molecule}$ are their molar masses. For the calculation of mean free paths, the diameters of the PbI$_2$ and MAI molecules are estimated based on the sum of the ionic radii of their individual elements.[77,78] Due to the larger diameter of the MAI molecule compared to PbI$_2$, a strong reduction of the

mean free path of MAI molecules is expected when increasing MAI partial pressure, whereas for equivalent MAI atmospheres, the mean free path of PbI$_2$ molecules is consistently two orders of magnitude higher than its MAI counterpart (see Figure 1b). As a consequence, within the optimum process regime for the fabrication of efficient perovskite thin films (here between 1 × 10^{-5} mbar and 5 × 10^{-5} mbar), the mean free path of MAI is expected to drop below 1 cm for MAI, whereas for PbI$_2$ it stays at values significantly above 20 cm and therefore above the typical distance between source and substrate. Based on these fundamental considerations, even for comparatively high MAI partial pressures the molecular flux of PbI$_2$ toward the substrate is still considered as a directed effusive flux and the evaporation rate to be constant within the relevant partial pressure range (and below). In contrast, evaporation of MAI is accompanied by a significant number of collisions between MAI molecules, resulting in a loss of the directed effusive flux and a transition to a more CVD-like evaporation behavior. Nevertheless, even if the MAI atmosphere is now considered as a residual background gas, a molecular flux rate of MAI from the background atmosphere toward the substrate is apparent according to the Hertz-Knudsen equation (see Equation (1), with a sticking coefficient α = 1). For the optimal process window for co-evaporation of PbI$_2$ and MAI, the flux of MAI molecules reaching the substrate is two orders of magnitude higher than that of PbI$_2$ molecules (with the sticking coefficient already being considered in the tooling factor). This is in agreement with the low sticking coefficient of MAI usually observed in literature (see Figure 1b).[79] Given similar chemical characteristics of related organic salts like methylammonium bromide (CH$_3$NH$_3$Br) or formamidinium iodide (CH(NH$_2$)$_2$I), significant CVD components are also expected for these materials. In that regard, similarly high partial pressures have been observed for these materials in primary studies by the authors.

Since the evaporation rate of MAI measured by a QCM in close proximity to the source is not expected to precisely reflect the exact amount of MAI in interaction with co-evaporated PbI$_2$, the process presented in this work (for further information about process and equipment details, the reader is referred to the Experimental Section) is controlled here by MAI partial pressure as measured close to the substrate, and with PbI$_2$ evaporation rate following previous approaches.[28–30,37,38] Considering the reduction in effusive flux of MAI, formation of the perovskite thin film on the substrate during co-evaporation is also influenced by delayed conversions of the effusively deposited PbI$_2$ film in the presence of the CVD-like background atmosphere of MAI. To highlight this conclusion, a surface conversion into perovskite of a thick pre-deposited PbI$_2$ film exposed to the MAI background atmosphere without any directed MAI flux reaching the film is presented in Figure S3, Supporting Information. Last but not least, decomposition of MAI into various decomposition products (primarily CH$_3$NH$_2$ and HI) was previously reported, whose reverse reactions at the substrate surface open up additional chemical reaction paths that shift the process mechanism further from a pure effusive to a more CVD-like process.[79] It remains an open question whether a pure effusive process or a mixture of effusive and CVD process is more beneficial for the fabrication of high-quality perovskite thin films. A
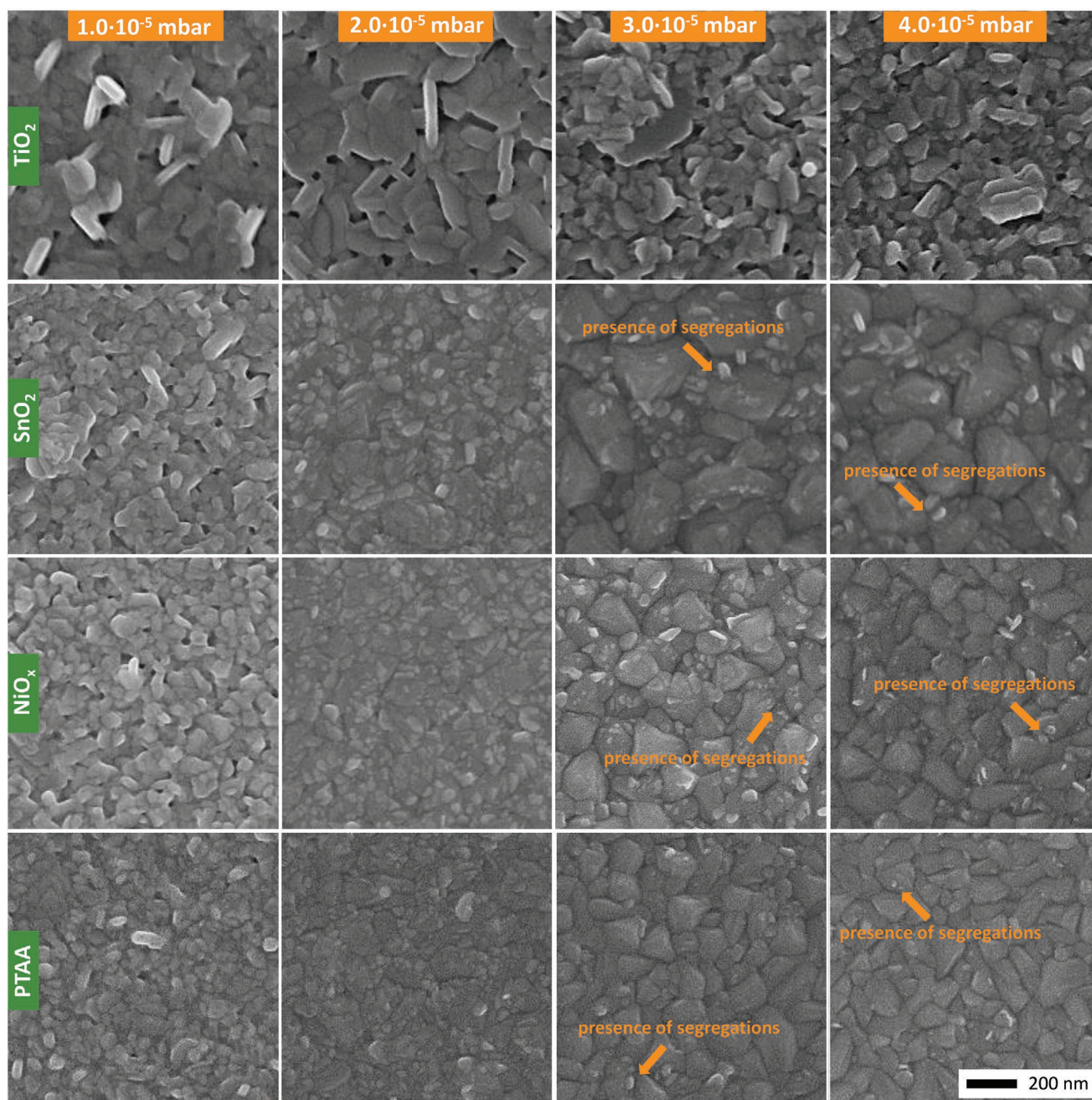
detrimental effect on uniformity is, however, not expected given the common application of CVD-like processes in industrial processes. Nevertheless, given the preceding discussion, both components need to be taken into account in the employed deposition process of this work. Considering these process characteristics and the various chemical reactions taking place directly at the substrate surface, the quality of the co-evaporated perovskite thin film is expected to particularly depend on the choice of substrate material, that is, its surface chemistry properties, as will be demonstrated and discussed in the following.

2.2. Interplay between Substrate Material and Thin-Film Formation during Co-Evaporation

This section demonstrates that the choice of substrate material is decisive for the chemical reaction between PbI_2 and MAI as well as the crystallographic properties of the co-evaporated perovskite thin film. To illustrate this, perovskite thin-film formation on the common charge transport materials titanium dioxide (TiO_2, n-type, solution-processed), tin dioxide (SnO_2, n-type, solution-processed), nickel oxide (NiO_x, p-type, vacuum-processed), and poly[bis(4-phenyl)(2,4,6-trimethylphenyl) amine] (PTAA, p-type solution-processed) is compared in scanning electron microscope (SEM) investigations (see **Figure 2**). Growth dynamics on a wide range of alternative organic and inorganic substrate materials (poly(3,4-ethylenedioxythiophene) polystyrene sulfonate (PEDOT:PSS), spiro-TTB, [6,6]-phenyl-C_{61}-butyric acid methyl ester (PCBM), poly(3-hexylthiophene-2,5-diyl) (P3HT), tungsten oxide (WO_x), and zinc oxide (ZnO)) are discussed in the Supporting Information to support the herein presented conclusions (see Figures S6 and S10, Supporting Information). Comparing surface morphology of thin films prepared at different MAI partial pressures, independent of the substrate material all perovskite thin films prepared at MAI partial pressures below 2×10^{-5} mbar show characteristic features of a PbI_2-rich composition—namely elongated, disc-shaped crystallite structures that result in defect-rich thin films with a high surface pinhole density. While increasing MAI partial pressure to above 2×10^{-5} mbar induces the formation of defined perovskite crystallites on SnO_2, NiO_x, as well as PTAA substrates, perovskite thin films deposited on TiO_2 always appear PbI_2-rich and show no defined grain structure (even for the highest MAI partial pressures). The latter observation is reinforced by the comparatively strong PbI_2 peaks observed in X-ray diffraction (XRD) investigations (see below). Further differences are apparent when comparing perovskite thin films deposited on SnO_2, NiO_x, and PTAA. Compared to the organic charge transport layer PTAA, perovskite thin films grown on the metal oxides SnO_2 and NiO_x also experience nonideal film formation to a lesser extent, as evident from the high density of segregations on the absorber surface forming even at the highest tested MAI partial pressures. These segregations are explained by either a phase with different stoichiometry or smaller perovskite grains. However, based on the needle-like structure of these segregations, a PbI_2-rich character is assumed here as has been previously reported.[80–83] Despite some uncertainties about the exact nature of these segregations, a rather detrimental influence is expected. Moreover, the size and

shape of perovskite crystals on PTAA appear more homogeneous and well defined. Although lateral grain sizes are slightly larger for thin films grown on top of SnO_2, grain sizes for all thin films fabricated in this study remain below 300 nm and consequently significantly below the values that are commonly achieved for solution-processed thin films.[84–87] Based on these observations, it is concluded that the substrate material strongly affects not only crystallographic properties of the perovskite crystallites, but also impacts the conversion of PbI_2 into perovskite and, thereby, the composition of the resultant perovskite thin film. This goes beyond previous studies, where detailed investigations showed that the substrate material can influence the composition and electronic structure of the perovskite thin film close to the underlying charge transport layer.[65–68] However, the present study supplements these findings by highlighting that, beyond the crystallization during the initial stage of thin-film formation, the incorporation of MAI into the perovskite framework, and thereby the composition of the perovskite, continuous to be influenced throughout the entire thin film.

In order to shed further light into the mechanism of nucleation and crystallization of perovskite thin films co-evaporated on different substrate materials, XRD investigations are performed (see **Figure 3**). The substrate materials TiO_2 and PTAA are highlighted here, as they have been previously discussed to exhibit the greatest differences (see Figure 2). X-ray diffractograms for perovskite thin films grown on SnO_2 and NiO_x can be found in the Supporting Information (see Figure S4, Supporting Information). In accordance with the SEM investigations, the incorporation of MAI into the perovskite framework is significantly hampered in the case of a deposition on top of TiO_2. While first perovskite peaks for thin films grown on top of PTAA arise at comparably low MAI partial pressures of 1×10^{-5} mbar (see Figure 3a), their formation appears at much higher MAI partial pressures $>3 \times 10^{-5}$ mbar in case of TiO_2 substrates (see Figure 3b). In addition, even for highest MAI partial pressures of 5×10^{-5} mbar, significant amounts of PbI_2 persist in these films. Independent of the substrate material, for all entirely converted perovskite thin films at MAI partial pressures of 5×10^{-5} mbar, a quasi-cubic rather than a tetragonal crystal structure is observed, as concluded from the missing peak splitting that is characteristic for the lower symmetry tetragonal structure (see, e.g., the (111) diffraction peak in Figure S5, Supporting Information), which has been observed before.[69,88] Furthermore, a clear difference in the dominant crystal orientation of the perovskite thin film is observed for different substrate materials, indicating a substrate-dependent texture effect. While thin films grown on top of TiO_2 and SnO_2 demonstrate dominant orientation along the {100} crystal planes, thin films grown on NiO_x and PTAA are more aligned along the {110} and {111} crystal planes (see Figure 3c). Considering that the XRD measurements were performed in Bragg-Brentano configuration, only diffraction arising from crystal planes perpendicular to the surface normal is detected, which implies that the unit cell must be tilted along its diagonal as shown in Figure 3d. Similarly, two distinct crystallographic scenarios are suggested for the alternative organic and inorganic materials investigated in this work (see Figure S6, Supporting Information). Perovskite thin films grown on top of P3HT, spiro-TTB, and to a lesser extent PCBM follow the behavior of thin films grown on PTAA and NiO_x with a preferred

**ADVANCED
SCIENCE NEWS**

www.advancedsciencenews.com

**ADVANCED
FUNCTIONAL
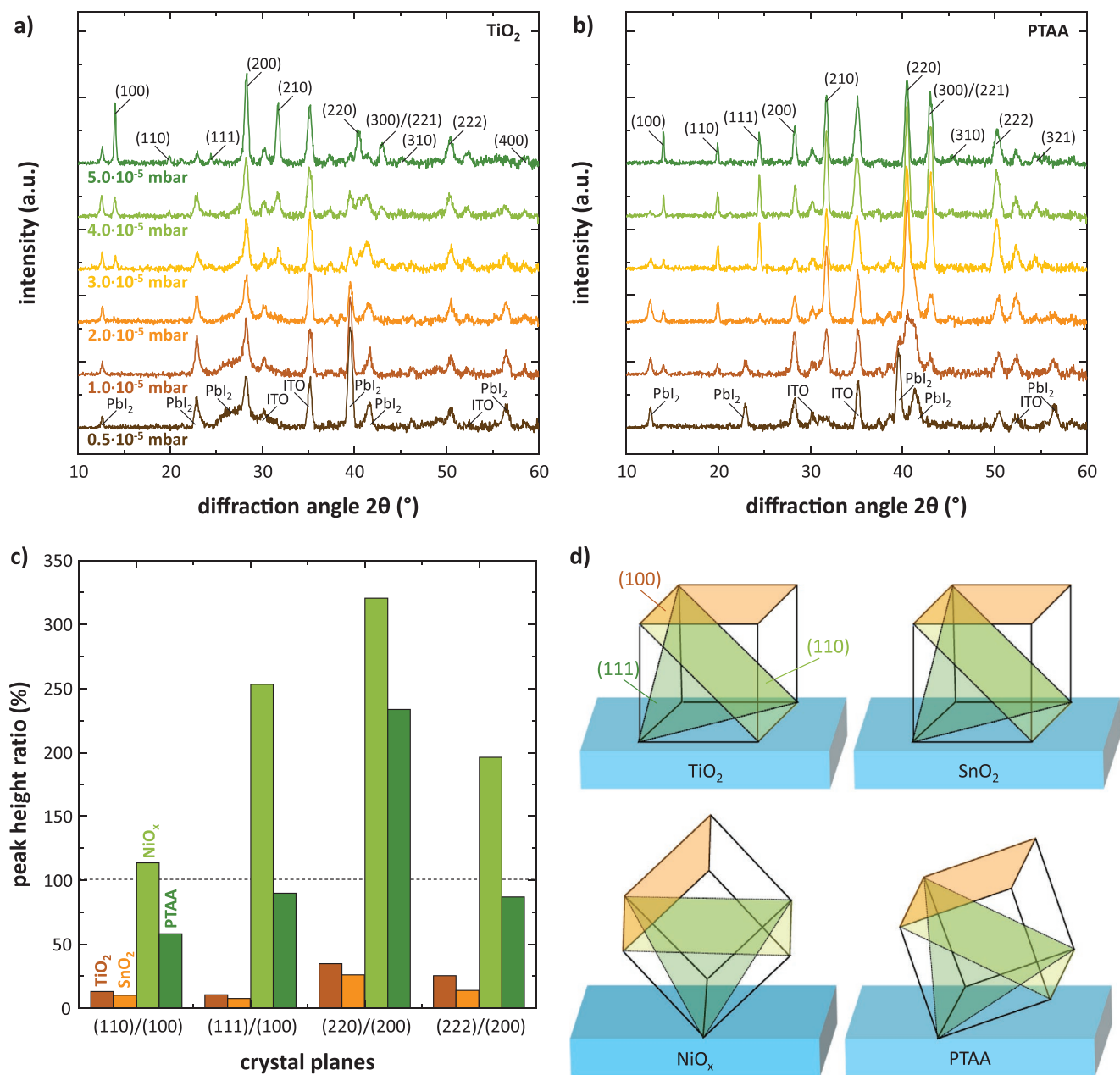MATERIALS**

www.afm-journal.de

Figure 2. Scanning electron microscope (SEM) investigations of perovskite thin films prepared at different MAI partial pressure during co-evaporation of PbI$_2$ and MAI on different charge transport materials. All perovskite thin films have a thickness of around 300 nm. The scale bar of all images is identical.

orientation along the {110} and {111} crystal planes, while the behavior of thin films on PEDOT:PSS, WO$_x$, and ZnO matches the general trends exhibited by the cases of TiO$_2$ and SnO$_2$. In this regard, thin films grown on top of WO$_x$ also indicate a delayed conversion as observed for TiO$_2$, given the weak and rather wide perovskite diffraction peaks as well the absorbers' visual appearance. The implications of these crystallographic differences are expected to have major impact on the exact crystallization mechanism and therefore the quality of the resulting perovskite thin film, which will be discussed in the following.

2.3. Basic Crystallization Model for Co-Evaporated Perovskite Thin Films

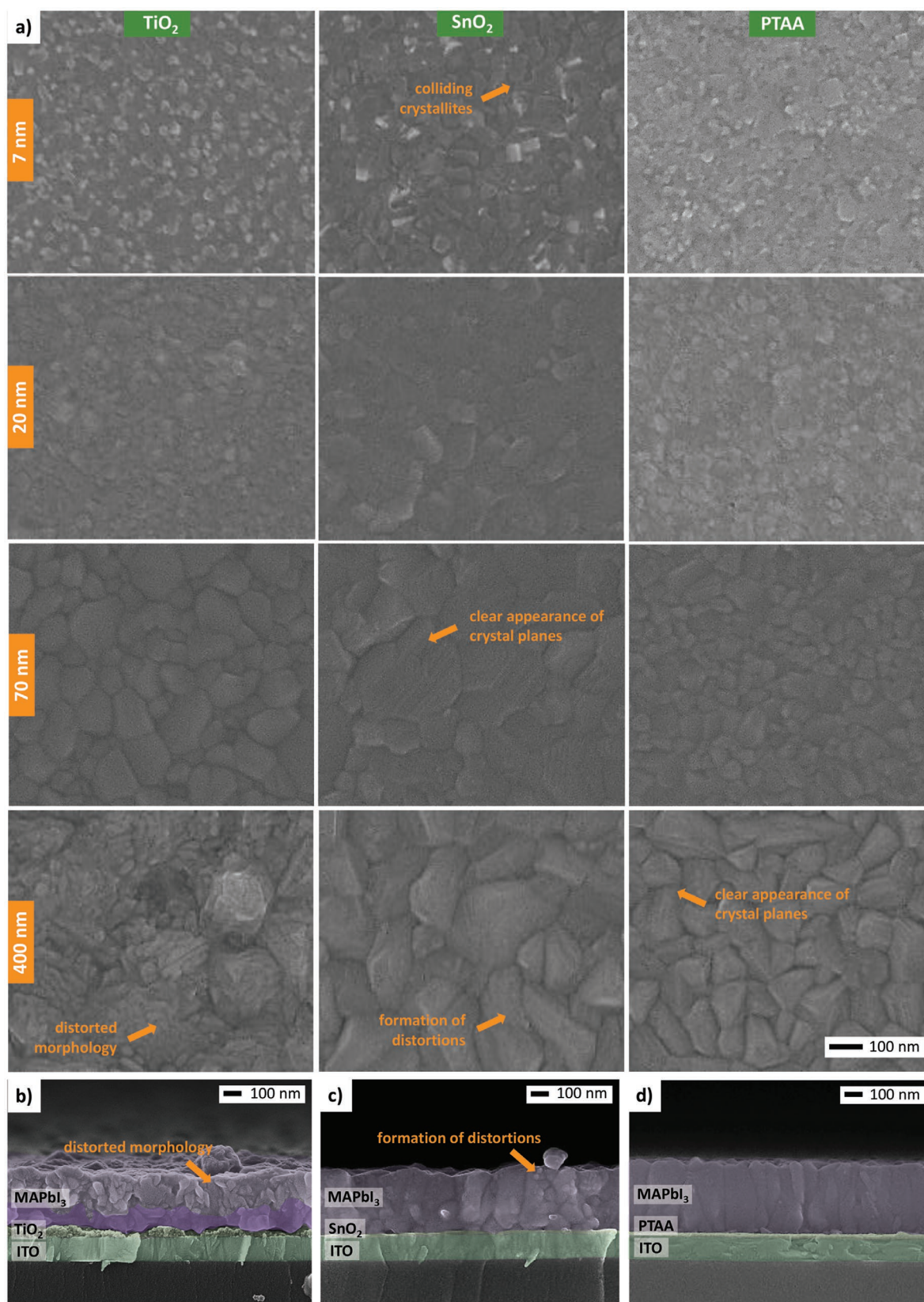Having highlighted strong differences in the morphology and composition of co-evaporated perovskite thin films grown on different substrate materials, further insights into the development of crystallization during the co-evaporation are presented here. The latter allows for the postulation of a basic crystallization model that describes the co-evaporation process employed here. Columnar grain growth is identified as highly substrate

**ADVANCED
SCIENCE NEWS**
www.advancedsciencenews.com

**ADVANCED
FUNCTIONAL
MATERIALS**
www.afm-journal.de

Figure 3. X-ray diffraction (XRD) investigations on perovskite absorbers grown on different substrate materials. X-ray diffractograms for absorbers grown at different MAI partial pressures on top of a) TiO$_2$ and b) PTAA. c) Ratio of the peak heights for the {100},{110}, and {111} crystal planes for absorbers grown on different substrate materials. d) Visual representation of the expected crystal orientation on different substrate materials.

dependent and as the key characteristic for high-quality co-evaporated perovskite absorbers. It is shown that the substrate material less influences the lateral grain growth (lateral grain size) but strongly the vertical grain growth and that only specific substrate materials allow for the desired case of vertically columnar grains ranging from one charge transport layer to the other. The implications of a columnar grain growth in vertical direction are further discussed in detail below. To study nucleation and crystallization dynamics during grain growth, the surface of the perovskite thin film is examined by interrupting the co-evaporation process at different stages of thin-film formation (see **Figure 4**a). The thickness of the

evaporated perovskite thin film is varied between 7 and 400 nm (by varying the thickness of the deposited PbI$_2$ layer between 5 and 300 nm, which is one of the control parameters of the co-evaporation process employed here as discussed in Section 2.1 and Experimental Section), which covers all stages of thin-film formation from nucleation to formation of a several hundred nanometer thick bulk layer. Degradation of the ultra-thin perovskite layers during handling and investigation was prevented by unloading samples via an inert environment and transferring samples in a special air-tight SEM sample holder. For all substrate materials, MAI partial pressure was fixed to 4×10^{-5} mbar. It is worth noting that the samples shown in

**ADVANCED
SCIENCE NEWS**

www.advancedsciencenews.com

**ADVANCED
FUNCTIONAL
MATERIALS**

www.afm-journal.de

Figure 4. Development of grain formation of co-evaporated perovskite absorbers on different substrate materials. a) Layer morphologies and crystallization process on different substrate materials in different stages of the co-evaporation process. All images have the same magnification. Cross-sectional SEM images of perovskite absorbers grown on b) TiO_2, c) SnO_2, and d) PTAA.
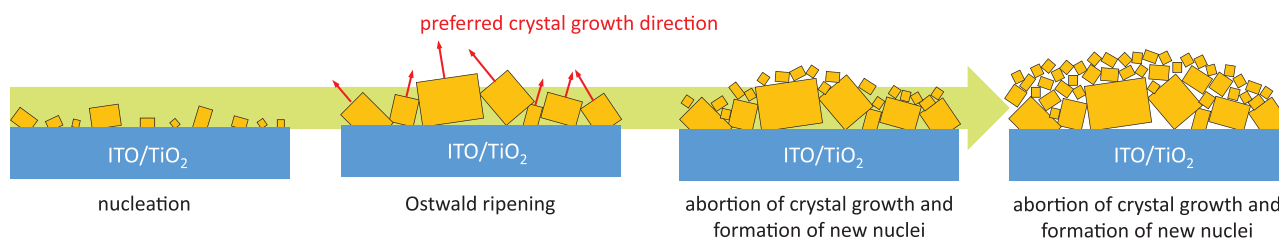
Figure 4 are prepared in a different evaporation run than in Figure 2. Due to the deposition around the optimal process conditions, slight variations in thin-film appearance (e.g., lower number of phase segregations) are expected as a result of minor changes in the process parameters (e.g., MAI partial pressure), which, however, do not interfere with the overall trends discussed before. Despite the fact that thick bulk layers showed significant visual differences for different substrate materials (see Figure 2), comparable behavior is observed in the initial stage of film formation for all three substrate materials investigated here, resulting in the formation of independent nuclei (see Figure S7, Supporting Information for larger images of the thinnest perovskite thin films). Considering further high-resolution XRD data, it is concluded that the composition of the perovskite thin films on the three investigated substrate materials is comparable in the initial stage of film formation, and that the presence of other dense layers such as crystalline PbI_2 is rather unlikely (see Figure S8, Supporting Information). However, compositional differences in the very first atomic layers (absorber thicknesses below 5 nm) as investigated in detail by Olthof et al. and others may still be present.[65–68] The density of initial nuclei is relatively large, with several nuclei being present with areas of a few 100×100 nm^2 in this stage. In particular, for SnO_2 substrates that exhibit slightly larger grain sizes compared to the other substrate materials in the early phase of the perovskite thin-film formation, a Volmer–Weber-like island growth mode for co-evaporated thin films can be concluded from the individual crystallites forming at this stage. A similar process has been concluded based on strain releasing effects observed in detailed XRD investigations by Parrott et al. that is proven here by direct observation for the first time.[69] As soon as a critical thickness is reached and these individual grains collide, an Ostwald ripening process takes place, which results in the coalescence of smaller into larger grains due to the lower thermodynamic stability of smaller grains, and in turn a reduction of the system's mean free energy.[89] While this process already takes place at thicknesses below 20 nm in the case of thin films grown on SnO_2, grain coalescence can be observed at thicknesses around 70 nm for thin films grown on TiO_2 and PTAA. The maximum grain size obtained in co-evaporated perovskite thin films is particularly defined in this step. In combination with the high density of nuclei it is speculated that this step is responsible for the most critical limitation of co-evaporated perovskite absorbers—the significantly smaller grain sizes compared to solution-processed absorbers. In contrast to solution-based deposition techniques, where nucleation is induced instantaneously by either annealing the wet film at high temperatures or by pouring orthogonal solvents onto the wet film, nucleation in vacuum processes is a rather slow process promoting the formation of a larger number of nuclei and, thus, smaller grains whose coalescence by the process Ostwald ripening is limited. This result goes beyond previous studies where the presence of an Ostwald ripening process was not taken into account.[69] Notably, large and defined grains are also apparent for thin films grown on TiO_2 in the initial stage of the film formation, even though the appearance of the thick bulk layer is significantly distorted. This observation is in line with the discussion above, stressing that the substrate material not only impacts nucleation and crystallization dynamics during
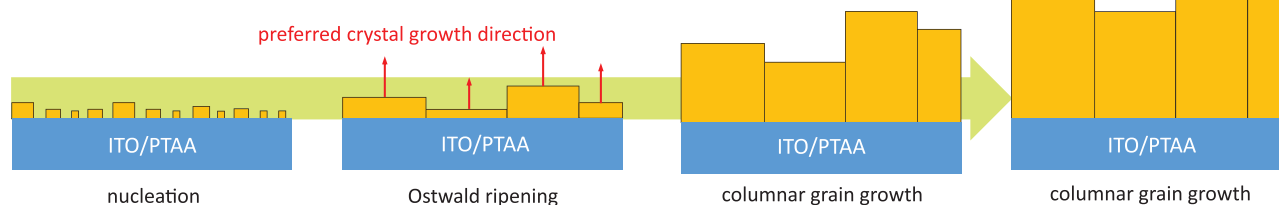
the initial stage of thin-film formation, but also causes significant distortions during the ongoing process (see also XRD study in Figure S8, Supporting Information). The latter results in a small-granular morphology with various horizontal grain boundaries along the direction of charge transport through the absorber (see Figure 4b), which are expected to have a detrimental effect on the electronic properties of solar cells—in particular fill factor (FF)—prepared with these absorbers (see also paragraph 2.4). Similarly, slight distortions with various phase segregations within the grains, along with horizontal grain boundaries, are also apparent in thin films grown on SnO_2 (see Figure 4c), in a much lower extent however, than for the case of TiO_2. Nevertheless, visible crystal planes within the perovskite grains are apparent even for thicker thin films, indicating a rather high quality of individual grains, at least for thicknesses of the perovskite thin film below 70 nm (see Figure 4a). In accordance with previous investigations, best morphological qualities are obtained for perovskite thin films grown on top of PTAA (see Figure 4c). For the employed co-evaporation process, PTAA allows for a dominant columnar crystal growth, apparent from the well-defined crystal planes and the homogeneous morphology both in horizontal as well as vertical direction, resulting in thin films with nearly no horizontal grain boundaries (see Figure 4d). This complements a homogeneous development of the composition of the perovskite thin film during grain growth as concluded from XPS investigations, while perovskite thin films on TiO_2 appear to become nitrogen-poor with passage of the deposition process (see Figure S9 and Table S1, Supporting Information). Perovskite thin-film morphologies without horizontal grain boundaries are commonly preferred, as charge transport is facilitated as discussed extensively in literature for a wide range of solution-processed perovskite thin films.[17,90–94]

In, general, the desired columnar grain growth appears to correlate to the difference in preferred crystal orientation, concluded by linking the differences in vertical grain growth to the results of the previous XRD investigation (see Figure 3 and discussion below). This conclusion is supported by the apparent correlation between preferred crystallographic orientation and vertical growth dynamics of the alternative substrate materials (see Figure S10, Supporting Information). Again, a distinct columnar grain growth is accompanied by a preferred orientation along the {110} and {111} crystal planes and, thus, is particularly observed for perovskite thin films grown on top of P3HT and spiro-TTB, while thin films on PEDOT:PSS and ZnO are well described by the behavior of thin films grown on top of SnO_2. A borderline case with a less pronounced columnar grain growth and a limited number of horizontal grain boundaries is observed for thin films grown on PCBM, which is in agreement with the less pronounced orientation along the {110} and {111} crystal planes for these thin films. Similar to the case of TiO_2 a strong distortion in morphology is observed for thin films grown on top of WO_x, which is further discussed in the following section. In summary, the employed substrate material is a crucial parameter of the co-evaporation process and obtaining a columnar grain growth—which is in turn connected to the choice of substrate material—a fundamental criterion toward the realization of efficient high-quality perovskite absorbers.

**ADVANCED
SCIENCE NEWS**

www.advancedsciencenews.com

**ADVANCED
FUNCTIONAL
MATERIALS**

www.afm-journal.de

a) growth on top of TiO₂-like subtrates

b) growth on top of PTAA-like subtrates

Figure 5. Basic crystallization model for the growth of co-evaporated perovskite absorbers on top of a) TiO₂-like substrates and b) PTAA-like substrates. For both scenarios only the case of an optimal MAI partial pressure is shown.

Based on the results of the SEM and XRD investigations, a basic crystallization model is postulated (see **Figure 5**). Detailed investigations performed so far have unveiled three distinct scenarios for the growth of perovskite thin films during co-evaporation, whose occurrence is highly depended on the employed substrate material: (1) a columnar grain growth mode (observed for PTAA, spiro-TTB, and P3HT), (2) a polycrystalline grain growth mode in vertical direction (observed for SnO₂, ZnO, and PEDOT:PSS), and (3) a highly distorted grain growth mode (observed for TiO₂ and WO$_x$), which can be considered as an extreme case of growth mode (2). In the following, two very distinct scenarios are depicted: the growth of the perovskite thin film on top of TiO₂ and on PTAA, with the first highlighting the case of a highly problematic growth dynamic and the latter the desired case, enabling high-quality co-evaporated perovskite thin films with a columnar grain structure (both cases are discussed at their individual optimal MAI partial pressure). As discussed above, the thin films exhibit a very similar growth characteristic during the first few nanometers on top of TiO₂ (see Figure 5a) and PTAA (see Figure 5b). In both cases, the formation of a relatively large number of nuclei is observed for layer thicknesses below 10 nm. As a result of the preferred reduction of the system's mean free energy, smaller grains coalesce and form grains with a grain size in the range of 100 to 200 nm (Ostwald ripening). While the behavior of systems with different substrate materials is similar until this point, crystallization differs significantly when a closed perovskite layer consisting of larger perovskite grains forms, as appears for a film thickness around 20 nm. Considering the XRD analysis, the dominant crystal orientation—also the preferred growth direction during film formation—differs (see Figure 3). In the case of samples grown on top of PTAA-like substrates a columnar grain growth dominates, allowing for a continuous growth of

the grains of the first entirely closed perovskite layer. Consequently, it is concluded that the preferred growth direction of these grains is perpendicular to the substrate surface. Grain growth of these perovskite grains must be preferentially perpendicular to the {110} and {111} crystal planes, which explains the stronger signal from these planes in the XRD diffractogram (see Figure 3). In contrast, for the case of perovskite thin films grown on top of TiO₂-like substrates, a preferred orientation of the {100} crystal planes was observed. Under the assumption that crystal growth takes place perpendicular to the {110} and {111} crystal planes, grains grown with a preferred {100} orientation will collide in the stage of the formation of an initial closed perovskite layer, preventing a further expansion of these grains. Under these circumstances, the system seems to have a preference to form new nuclei that coalesce into smaller grains, explaining the continuously smaller grains when moving away from the substrate. Additionally, the incorporation of MAI into these secondary grains is significantly hampered, resulting in delayed conversion into perovskite even at higher MAI partial pressures—at least in the capping layer (see also development of XRD peaks in Figure S8, Supporting Information). An interesting question for following investigations is whether external factors such as temperature are able to impact crystal orientation toward a more columnar grain growth even for substrates that do not show an intrinsic drive for a columnar grain growth. Also, the process of Ostwald ripening is known to be highly dependent on temperature which might open up suitable methods to tune grain size in co-evaporated perovskite solar cells.[95,96] With the basic crystallization model, a first connection between growth dynamics and the quality of the co-evaporated perovskite thin film is provided. Next, the key characteristics of the substrate material, which enable a columnar grain growth and thus high-quality perovskite thin films, are discussed.
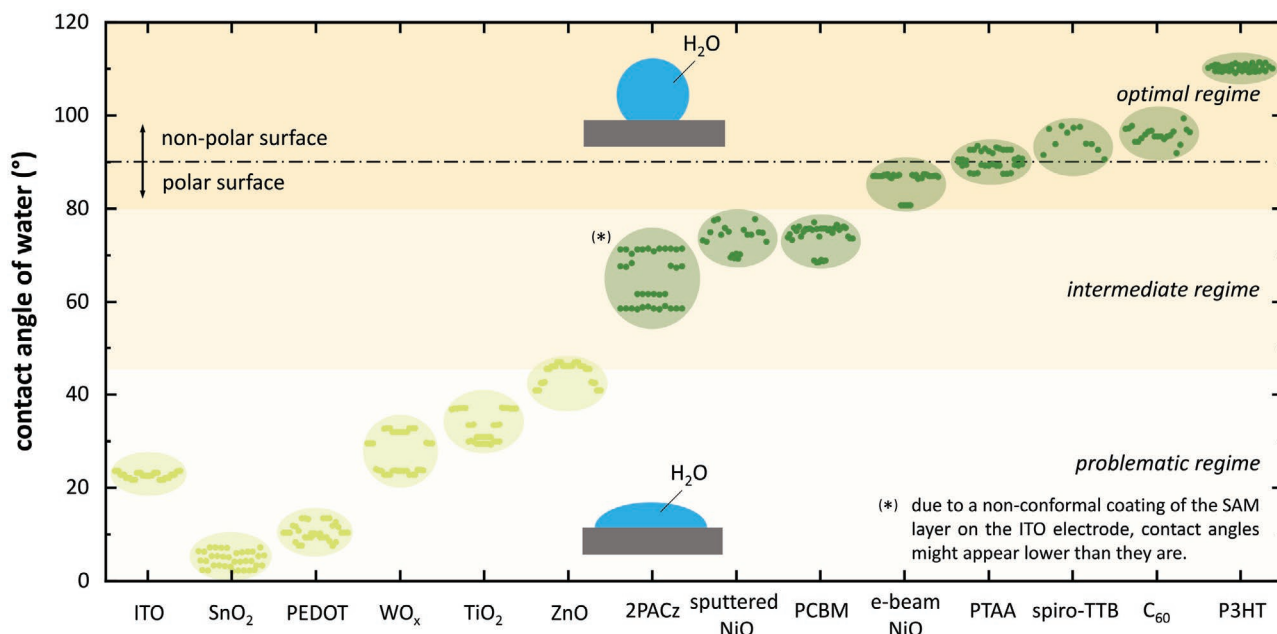
Figure 6. Investigation of the surface polarity of commonly employed charge transport layers by water contact angle measurements. All charge transport materials were deposited on top of an ITO front electrode. Substrates not fabricated by vacuum-based methods were kept in vacuum ($<5 \times 10^{-7}$ mbar) overnight to simulate a more realistic scenario for vacuum-processed perovskite solar cells. For every substrate material several individual measurements were performed.

2.4. Substrate Guidelines for Efficient Co-Evaporated Perovskite Solar Cells

Having highlighted the differences in growth dynamics of co-evaporated perovskite thin films on top of different substrate materials and identified columnar grain growth as a crucial characteristic toward high-quality perovskite thin films, a guideline for the choice of substrate materials for the fabrication of efficient co-evaporated perovskite solar cells is developed. It is shown that the surface polarity of the substrate material is the driving force for columnar grain growth and that non-polar substrate surfaces are preferable. For this, additional characterization is performed on the substrate materials employed in this study, as well as materials that were used in literature previously or have the potential to be of serious interest for the co-evaporation of perovskite absorbers in the future. Crystallinity and morphology of the vacuum-deposited perovskite thin film depend on the roughness of the substrate material on one side, and its surface energy on the other. In addition, an effect on the composition of the absorber can arise from catalytic reactions between the deposited absorber and the adjacent interface as is known, for example, for perovskite thin films in contact with TiO_2, ZnO, or NiO_x.[67,97–100] A clear difference between substrate materials is observed in the surface polarity as extracted from contact angle measurements (see **Figure 6**). It should be noted that measurements of surface properties (e.g., polarity) are in general difficult since every measurement at the surface results in a change of the surface itself. Therefore, special care has to be taken when performing and interpreting measurements of surface characteristics. In terms of contact angle measurements performed in this work, validity of the investigation is assured by: (1) performing contact angle measurements for accurate

surface conditions by keeping substrates not fabricated via vacuum-based methods in vacuum overnight, which is a more realistic scenario for vacuum-processed perovskite solar cells (see Figure S11, Supporting Information), and (2) by employing a high-speed camera in the setup that allows for extraction of the contact angle before detrimental water-surface interactions set in (see Figure S12, Supporting Information). In general, the focus of the following contact angle study is rather on the overall trend between different substrate materials than on the absolute value. Especially for the metal oxides TiO_2, SnO_2, ZnO, and WO_x as well as the organic material PEDOT:PSS a strong polarity of the surface is apparent, with contact angles below 50°. In contrast, for substrates coated with PTAA, spiro-TTB, or P3HT, which resulted in the best perovskite thin film quality with a pronounced columnar grain growth, contact angles close to 90° or above indicate a non-polar surface. It is postulated that these differences in surface polarity are mainly responsible for differences in crystallization dynamics—that is, the difference in preferred crystal growth direction defining the final morphology—in co-evaporated perovskite thin films and that high-quality thin films require a careful optimization of the underlying surface. In fact, it is expected that differences in surface polarity of the substrate material have a distinct influence on the chemical alignment and incorporation of vacuum-deposited (polar) molecules, which in turn result in differences in composition and crystal orientation.

The model traces a variety of empirical substrate-related effects reported in literature to a single cause, namely the polarity of the substrate. For the first time, this study explains why co-evaporated perovskite absorber grown on organic substrate materials, which usually result in non-polar surfaces, outperform any absorber grown on top of a polar metal oxide.

This is in stark contrast to solution-based approaches, where wetting of the perovskite solution on the substrate surface is most decisive parameter, which is however tunable by different approaches, allowing a larger variety of employable substrate materials.[86,101–104] PEDOT:PSS with its highly polar surface is an exception and has been shown previously to result in rather limited performance for evaporated perovskite solar cells.[105] In fact, efficient co-evaporated absorbers grown on a metal oxide are usually equipped with an additional fullerene interface layer (e.g., C_{60} or PCBM),[40,62,68,71] which is shown here to convert the polar surface of the metal oxide into a less-polar surface and therefore promote a columnar grain growth. However, it is expected that these approaches are not yet fully exploited since PCBM is still slightly off the optimal process regime (see also Figure S10, Supporting Information). Additionally, it should be noted that the exact surface state of the substrate material can highly depend on the exact fabrication method, as has been previously shown for example for the case of TiO_2 in literature.[67] Similarly, it is shown here that a strong difference in surface polarity for NiO_x films prepared via either sputtering or electron-beam evaporation is present, with a much lower surface polarity for the latter case, opening up a promising route toward efficient co-evaporated absorbers grown on a metal oxide. This route manifests itself in the previous demonstration of efficient and stable co-evaporated absorbers grown on electron-beam-evaporated NiO_x.[37,38] Based on the performed surface investigation, solution-processed self-assembling monolayers based on [2-(9H-carbazol-9-yl)ethyl]phosphonic acid (2PACz) that have recently been developed for solution-based single- and multijunction perovskite solar cells are identified as another promising substrate material candidates for co-evaporated perovskite.[60,106] In fact, the latter has been demonstrated recently to result in high-efficiency co-evaporated perovskite absorbers.[107] As a proof of principle for the developed substrate guideline and the distinct link between surface polarity, crystallization dynamics, and finally device performance, the use of vacuum-processable spiro-TTB is shown to result in efficient all-evaporated perovskite solar cells in the following section.

The apparent correlation between surface polarity and crystallization dynamics of co-evaporated perovskite thin films is evident for the vast majority of the investigated substrate materials. Exceptions are limited to comparably rough but polar TiO_2 and WO_x substrates prepared from nanoparticle solutions (see cross-sectional images in Figure 4 and Figure S10, Supporting Information as well as atomic force microscopy images in Figure S13, Supporting Information). Crystallization dynamics of co-evaporated perovskite thin films prepared on these rougher substrates is shown above to be hampered, highlighting that the guideline proposed herein is most valid for planar surfaces. A more complex behavior is expected for rough substrates, which might also explain the usually lower quality of co-evaporated perovskite thin films on top of textured surfaces.[38,62,64] However, even for perovskite thin films deposited on top of TiO_2 substrates with their larger roughness, polarity strongly impacts crystallization dynamics as shown in an additional experiment using a spiro-TTP interlayer in between the perovskite absorber and the TiO_2 substrate (see Figure S14, Supporting Information).

Having discussed the interplay between substrate material and crystallization dynamics of co-evaporated perovskite thin films in detail, the performance of solar cells fabricated with perovskite thin films grown on different substrate materials are shown and correlated to the observations made before. In agreement with the previous discussion, a distinct correlation between surface properties of the substrate material, quality of crystallization, and performance of the resulting solar cells is apparent. **Figure 7** summarizes the main solar cell parameters for co-evaporated absorbers grown on the different substrate materials at different MAI partial pressures. In accordance with the XRD investigation (see Figure 3) an improved conversion of PbI_2 into perovskite is apparent with increasing MAI partial pressure, resulting in an increase in short-circuit current density (J_{sc}). In particular, a strong increase in J_{sc} with the MAI partial pressure is observed for absorbers grown on SnO_2 and PTAA, while absorbers grown on NiO_x indicate a slight delay in conversion, especially for lower MAI partial pressures, resulting in a comparatively small process window in which efficient solar cells are prepared (see Figure 7d). In contrast, the conversion for absorbers grown on TiO_2 is significantly hampered, in agreement with the results from previous XRD and SEM investigations. This again highlights the substantial influence of substrate material on the final stoichiometry of the co-evaporated perovskite thin film and in turn on the charge carrier generation in the absorber. The general trends in charge carrier generation, including the maximum achieved values for J_{sc}, are also confirmed by the optical properties of perovskite absorbers grown on different substrates (see Figure S15, Supporting Information). Furthermore, the trend in J_{sc} is reflected in the PCE of solar cells prepared on different substrate materials (see Figure 7a). However, next to the inevitable influence of J_{sc} on PCE, additional effects arise from differences in the effectivity of charge transport through the absorber, which are described by the fill factor (FF) (see Figure 7c). As hypothesized before, highest FFs are achieved for absorbers exhibiting a columnar grain structure with a reduced number of horizontal grain boundaries, as achieved for absorbers on less polar to non-polar substrates such as NiO_x and PTAA. Combining the facilitated incorporation of MAI into the perovskite framework with preferential columnar grain growth, solar cells with PCEs exceeding 17.5% are demonstrated for absorbers grown on PTAA substrates. Absorbers grown on top of NiO_x, which showed a slight delay in MAI incorporation and therefore lower J_{sc} values, achieve slightly lower values akin to those of SnO_2, with its fast conversion into perovskite but disturbed grain structure (see Figure S16, Supporting Information). Further fine-tuning in terms of composition and thickness for absorbers grown on PTAA enables even higher PCEs up to 18.4% in the J–V-scan with stabilized PCEs of 18.1% (see Figure S17, Supporting Information). Open-circuit voltages (V_{oc}) for working solar cells differ only marginally between the different configurations. However, slightly higher V_{oc} values are observed for absorbers that are nominal PbI_2-rich—including all samples prepared on TiO_2 substrates. A similar enhancement in V_{oc} was reported for solution-based approaches and is associated with a defect passivation in PbI_2-rich perovskite absorbers.[108–110] It should be noted that differences in V_{oc} can also arise from voltage losses caused by charge transport limitations due to non-ideal charge transport layers. However, severe limitations of the charge transport layers are
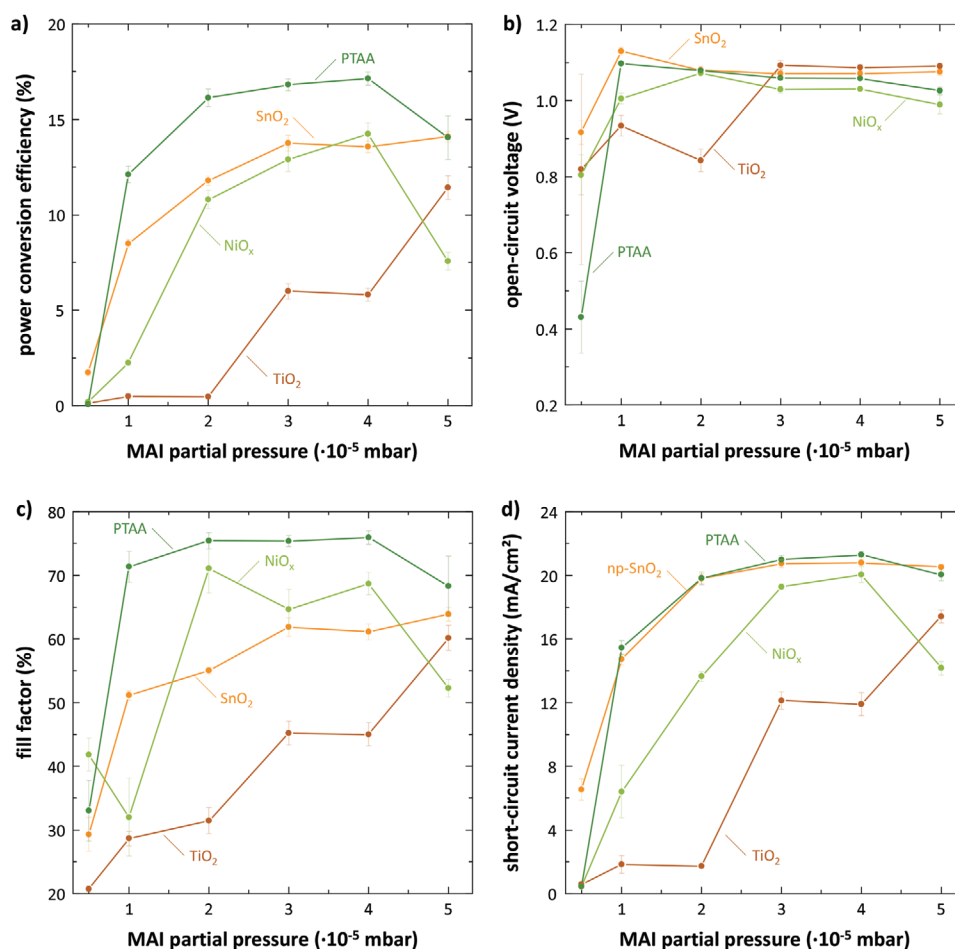
Figure 7. Performance of solar cells based on perovskite thin films grown on different substrate materials at different MAI partial pressures. a) Power conversion efficiency (PCE), b) open-circuit-voltage (V_{oc}), c) fill factor (FF), and d) short-circuit current density (J_{sc}). Shown are the mean values of 16 solar cells each together with their respective standard deviation.
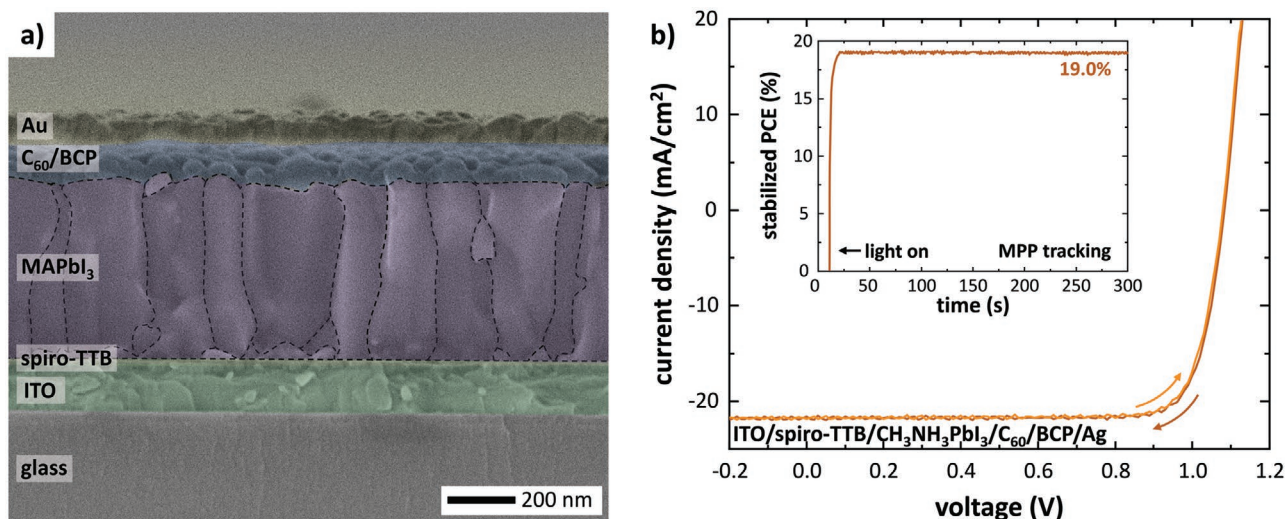
excluded here as the main cause for the observed differences since all charge transport materials have been previously used and proven to be efficient.[111–113] In general, the process window for MAI partial pressure in which working devices are prepared is rather similar, with values between 3×10^{-5} mbar and 4×10^{-5} mbar, showing that the device performance cannot be further improved significantly and is restricted by the limitations in stoichiometry as well as morphology. Especially for perovskite thin films grown on PTAA and NiO$_x$, higher MAI partial pressures result in a reduction in J_{sc} and FF which is related to a MAI-rich composition as previously reported.[107]

Next to the PCEs of these devices, device stability is affected by the differences in perovskite thin film stoichiometry and morphology (see Figure S18, Supporting Information). In particular, stable and hysteresis-free devices with stabilized PCEs close to the values extracted from J–V-scans are again achieved for absorbers grown on top of PTAA. In addition, devices grown on top of SnO$_2$ also exhibit stable power output during prolonged maximum power point (MPP) tracking. However, due to their comparatively strong hysteresis, this is with significantly lower values than were achieved in the J–V-scans. Devices prepared on NiO$_x$ and especially on TiO$_2$ do not stabilize during

MPP tracking, which is linked to a disturbed stoichiometry occurring as a result of the insufficient incorporation of MAI into the perovskite framework. It has also been shown by Patel et al. that the substrate material which the co-evaporated perovskite absorber is deposited onto can influence hysteric behavior by inducing changes at the interface toward the substrate.[68] This observation is complemented here by a detected influence of the substrate material also on crystallographic and morphological properties throughout the entire absorber. Having shown a distinct relationship between the performance of co-evaporated perovskite absorbers prepared on different substrate materials, their specific surface properties, and the fundamental processes during perovskite thin-film formation, the developed guidelines allow for an effective approach in the selection and development of novel efficient substrate materials, which is demonstrated in the following proof of concept.

2.5. Toward Efficient All-Evaporated Perovskite Solar Cells

Building on the selection criteria for the substrate material discussed above, efficient all-evaporated perovskite solar cells are

**ADVANCED
SCIENCE NEWS**
www.advancedsciencenews.com

**ADVANCED
FUNCTIONAL
MATERIALS**
www.afm-journal.de

Figure 8. Efficient all-evaporated perovskite solar cells by careful substrate choice. a) Cross-sectional SEM image of a co-evaporated perovskite solar cell employing spiro-TTB as hole extraction layer. Clearly visible grain boundaries have been highlighted. b) J–V-characteristic and performance under continuous illumination under MPP tracking conditions of a typical all-evaporated perovskite solar cell employing spiro-TTB.

presented by introducing a vacuum-processable HTL with a non-polar surface into the layer stack sequence. An ultra-thin undoped spiro-TTB is employed as an efficient vacuum-processable alternative to the solution-based HTL PTAA that was shown to be an ideal choice for the fabrication of high-quality co-evaporated perovskite thin films due to its non-polar surface properties (see Figure 6) that facilitate an efficient crystallization of the co-evaporated thin film. Spiro-TTB was used in all-evaporated perovskite solar cells by Polander et al. as a triple-layer HTL, consisting of a thin dopant layer followed by a thicker doped and a undoped spiro-TTB layer, however, with only decent performances.[114] In addition, spiro-TTB was also employed in tandem solar cell stacks processed via hybrid fabrication methods with different film formation dynamics.[58,115] Based on these promising results, an optimized and simplified architecture based on the layer stack sequence glass/ITO/spiro-TTB/$CH_3NH_3PbI_3$/C_{60}/BCP/Ag employing only an ultra-thin (<3 nm) undoped spiro-TTB layer is adapted for all-evaporated perovskite solar cells (see **Figure 8**). The co-evaporation of the perovskite absorber in this layer stack sequence results in the desired homogenous columnar grain growth of the perovskite thin film as expected from the surface investigation (see Figure 8a). The resulting all-vacuum-processed perovskite solar cells reach stabilized PCEs of up to 19% (see Figure 8b), being a significant progress compared to the original work by Polander et al., which is due to an enhancement in all J–V-parameters. This is explained by the simplified device architecture on the HTL side as well as the addition of a thin BCP layer between the C_{60} layer and the rear electrode, both enabling better charge carrier transport and extraction and therefore improved values for FF and V_{oc}. These devices are among the best reported all-evaporated perovskite solar cells without a solvent-based step in any of the utilized functional layers, achieving state-of-the-art PCEs above 19%.[23,24,39,41,116] It is worth noting that with only one undoped ultra-thin charge transport layer on the substrate side, the complexity

of the employed layer stack sequence is significantly reduced compared to previously discussed all-evaporated layer stacks relaying on multi-layer charge transport materials.[34,114,117] The champion device prepared in this configuration achieves a PCE of 19.5%, an V_{oc} of 1.08 V, a FF of 83.0%, and a J_{sc} of 21.6 mA cm^{-2} in backward scan direction and a PCE of 19.3%, an V_{oc} of 1.08 V, a FF of 81.7%, and a J_{sc} of 21.9 mA cm^{-2} in forward scan direction, highlighting the low hysteresis observed in these devices. J_{sc} values extracted from external quantum efficiency (EQE) measurements are in good agreement with the values of the J–V-scans (see Figure S19, Supporting Information). In addition, good performance is achieved during MPP tracking under continuous AM1.5g illumination over a prolonged time of several days, similar to previously reported all-evaporated perovskite solar cells (see Figure S20, Supporting Information)[34] as well as good reproducibility of the process, which is apparent from the low standard deviation in the parameters of more than 300 solar cells fabricated in 24 consecutive deposition runs (see Figure S21, Supporting Information). Based on the realization of efficient all-evaporated perovskite solar cells, it is shown that the developed substrate guidelines are indeed able to screen out promising substrate materials that are worth optimizing the perovskite absorber deposition on, as well as to rediscover promising charge transport materials like spiro-TTB that had already been introduced for all-evaporated perovskite solar cells in literature, but fell into oblivion shortly after introduction due to alternative upcoming materials. It is expected that the optimized layer stack and the use of undoped spiro-TTB as an efficient hole transport material is of particular interest for the further development of vacuum-processed perovskite solar cells. Due to the ease of upscaling, conformal coating on rough and textured surfaces, high reproducibility, and the outstanding production yield of vacuum-based fabrication methods, they are considered to play a particular role in the development of large-area perovskite solar modules and the integration of fully vacuum-processed perovskite solar cells into

multi-junction solar cell applications. In that regard, first promising results in terms of upscaling of the deposition processes to larger areas have already been reported recently.[37,71,118,119]

3. Conclusion

This work reports on how important the choice of the substrate material is for the crystallization dynamics of co-evaporated thin films for perovskite PV. The substrate material affects not only crystallographic and morphological properties of the resulting perovskite thin film, but also the incorporation of MAI into the perovskite framework and, therefore, the stoichiometry of the thin films. Based on detailed break-off experiments all relevant stages of the nucleation and crystallization of co-evaporated thin films on different substrate materials are examined, which allows postulating of a basic crystallization model for co-evaporated perovskite thin films. Independently of the substrate material, a high density of nuclei is observed, which likely causes the small grain size typically achieved for co-evaporated perovskite thin films. During the initial stage of the layer formation, a Volmer-Weber-like island growth mode takes place, accompanied by an increase in grain size via the Ostwald ripening mechanism. While defined perovskite grains are apparent for all investigated substrate materials in this initial stage, the ensuing growth dynamics are highly dependent on the underlying substrate material. A beneficial columnar grain growth resulting in a low number of horizonal grain boundaries is observed only for specific substrate materials with well-defined surface properties. As main substrate characteristic in order to achieve the desired columnar grain growth, non-polar substrate surfaces are identified, which explains the rather limited number of substrate materials employed for efficient vacuum-processed perovskite solar cells in literature in contrast to the vast variety of substrate materials in solution-based approaches. Furthermore, efficient and stable perovskite solar cells with PCEs above 19% are achieved for substrate materials that allow for a homogeneous and columnar grain growth of the perovskite thin film and, thus, only after careful choice and adjustment of the substrate material. Finally, the organic vacuum-processable hole transport material spiro-TTB is shown to be an ideal candidate for the fabrication of efficient all-evaporated perovskite solar cells that keep pace with the commonly employed mixed solution- and vacuum-based layer stack sequences. Following investigations have to clarify whether the discovered correlations between substrate material and device morphology as well as performance are limited to the exact fabrication technique as well as employed absorber composition.

4. Experimental Section

Substrate Preparation: Glass substrates coated with pre-patterned indium tin oxide (ITO, Luminescence Technology, CAS: 50926-11-9) were cleaned in acetone and isopropanol in an ultrasonic bath for 10 min each, followed by an additional cleaning step in an oxygen plasma for 3 min immediately before the deposition of the charge transport layers. For devices in n-i-p architecture either solution-processed tin dioxide (SnO_2) or titanium dioxide (TiO_2) in nanoparticular form were employed as electron transport material. The nanoparticular SnO_2 layer was fabricated via a solution-based approach as discussed in a previous report.[112] For this, a commercial SnO_2 colloidal dispersion (15 wt% dispersion, Alfa Aesar, CAS: 18282-10-5) was diluted in deionized water to a concentration of 2 wt%. The deposition of the solution on top of the ITO front electrode was performed by spin coating at 4,000 rpm for 30 s followed by an annealing step at 250 °C for 30 min in air. The TiO_2 layer was prepared according to a previous report.[11] The self-synthesized nanoparticular solution was spin-coated at 7,000 rpm for 30 s and annealed at 100 °C for 30 min in air. Both layers have a thickness of around 20 nm. For devices in p-i-n architecture either solution-processed PTAA, sputtered nickel oxide (NiO_x), or thermally evaporated spiro-TTB were used as hole transport layer. PTAA (EM Index Co. Ltd., CAS: 1333317-99-9) was dissolved in anhydrous toluene (99.8%, Sigma Aldrich, CAS: 108-88-3) with a concentration of 0.8 mg mL^{-1} and spin-coated for 30 s at a rotation speed of 5,000 rpm in a nitrogen-filled glovebox. The resulting layer had a thickness below 5 nm. In order to remove residual solvents inside the film, a drying step at 100 °C for 10 min was employed. Sputtering of the NiO_x layer was performed in a PVD 75 Pro-Line sputter system (Kurt J. Lesker Company) by employing a green NiO target (99.995% purity, Kurt J. Lesker Company, CAS: 1313-99-1) that was sputtered in a pure argon atmosphere at a process pressure of 1 mTorr and a power of 8 W in^{-2}. The thickness of the NiO_x layer was around 20 nm. Electron-beam-evaporated NiO_x was fabricated as described previously.[37] The 3 nm thick spiro-TTB layer (Luminescence Technology, CAS: 515834-67-0) was thermally evaporated in a Spectros evaporation system (Kurt J. Lekser Company) without any doping. Self-assembling monolayers based on [2-(9H-carbazol-9-yl) ethyl]phosphonic acid (2PACz) were prepared by dissolving 1.5 mg of 2PACz (98% purity, TCI Deutschland GmbH, CAS: 20999-38-6) in 4 mL of anhydrous ethanol (99.5%, Sigma Aldrich, CAS: 64-17-5) and kept in ultrasound for 20 min. Spin coating was performed for 30 s at a rotation speed of 3,000 rpm in a nitrogen-filled glovebox followed by an annealing step at 100 °C for 10 min. All alternative substrate materials poly(3,4-ethylenedioxythiophene) polystyrene sulfonate (PEDOT:PSS), [6,6]-phenyl-C$_{61}$-butyric acid methyl ester (PCBM), poly(3-hexylthiophene-2,5-diyl) (P3HT), tungsten oxide (WO_x), and zinc oxide (ZnO) were fabricated via solution-based processes. PEDOT:PSS (Heraeus CLEVIOS P VP 4083, CAS: 155090-83-8) dispersed in water was filtered, diluted with deionized water (1:1 volume ratio), and spin-coated at a rotation speed of 4,000 rpm for 30 s in air followed by an annealing step at 150 °C for 30 min also in air. PCBM (Solenne BV, CAS: 160848-22-6) was dissolved in 1,2-dichlorobenzene (99% anhydrous, Sigma Aldrich, CAS: 64-17-5) with a concentration of 20 mg mL^{-1} and spin-coated at a rotation speed of 4,000 rpm for 30 s in a nitrogen-filled glovebox followed by an annealing at 80 °C for 30 min in nitrogen. P3HT (Sigma Aldrich, CAS: 156074-98-5) was dissolved in chlorobenzene (99.8% anhydrous, Sigma Aldrich, CAS: 108-90-7) and spin-coated at a rotation speed of 4,000 rpm for 30 s and annealed at 100 °C for 30 min both in a nitrogen-filled glovebox. For both ZnO (2.5 wt%, Avantama AG, CAS: 1314-13-2) and WO_x (2.5 wt%, Avantama AG, CAS: 1314-35-8), commercially available colloidal dispersions in isopropanol were used. The dispersions were spin-coated in a nitrogen-filled glovebox at a rotation speed of 4,000 rpm for 30 s and annealed at 100 °C for 30 min in nitrogen.

Absorber Fabrication: Before the co-evaporation of the $CH_3NH_3PbI_3$ absorber layer, no additional treatment of the surface was performed. For the purpose of outgassing, the substrates were left in the load-lock chamber of the evaporation system and kept in high-vacuum overnight. Methylammonium iodide (CH_3NH_3I, GreatCell Solar, CAS: 14965-49-2) was replaced after every evaporation run and also kept for outgassing overnight. Lead iodide (PbI_2, Sigma Aldrich (99%), CAS: 10101-63-0) was used in several consecutive evaporation runs employing a 3-h outgassing step for fresh PbI_2 at temperatures of ≈300 °C. The evaporation system was homemade with an Agilent Turbo-V 551 Navigator turbomolecular pump (with Holweck stage) and an Agilent IDP-15 dry scroll pump for the vacuum generation. Stable MAI partial pressures were obtained by adding an elbow flange in front of the inlet of the turbomolecular pump that reduces pumping speed.

The low-temperature evaporation sources were also homemade, utilizing molybdenum heating wires and quartz glass crucibles for the source materials. The composition of absorbers was controlled by the evaporation rate of PbI_2, which was held at 0.5 Å s^{-1}, and the partial pressure of the CH_3NH_3I, which was varied in the range between 1×10^{-5} mbar and 5×10^{-5} mbar. The rate of the PbI_2 evaporation was controlled by means of a 6 MHz QCM (INFICON, SQM-242) placed in close proximity to the PbI_2 evaporation source, the MAI partial pressure by employing a full-range Pirani/inverted magnetron pressure gauge (Varian, FRG-700) situated far from the evaporation sources. Since the evaporation of PbI_2 can be considered to be purely effusive, PbI_2 does not contribute to the measured background pressure, which lays two orders of magnitude above the base pressure. Before opening the substrate shutter, a constant PbI_2 evaporation rate and MAI background pressure were set by slowly ramping up the temperature of the evaporation sources, usually requiring 1 h of pre-deposition. During the deposition, substrates were not actively cooled nor heated. For the pressure series, absorbers that would be made into solar cells were rinsed in isopropanol and dried in nitrogen to remove residual CH_3NH_3I on top of the perovskite thin film immediately prior to depositing the charge extraction layer. However, absorbers prepared for surface characterization and absorbers integrated into the all-evaporated solar cell layer stack did not undergo this step. For further information about the co-evaporation process, the reader is referred to previous reports.[37,38]

Solar Cell Fabrication: Solar cells in n-i-p architecture were equipped with a doped 2,2",7,7"-tetrakis[*N,N*-di(4-methoxyphenyl)amino]-9,9'-spirobifluorene (spiro-MeOTAD) layer as the hole transport layer. For this, 80 mg mL^{-1} of spiro-MeOTAD (Luminescence Technology Corp., CAS: 207739-72-8) was dissolved in chlorobenzene. After complete dissolution, 28.5 µL of 4-tert-butylpyridine (98% purity, Sigma Aldrich, CAS: 3978-81-2) and 17.5 µL of a lithium stock solution were added to the solution. The lithium stock solution was prepared by dissolving 520 mg of bis(trifluoromethanesulfonyl)imide (Sigma Aldrich, CAS: 90076-65-6) in 1 mL of acetonitrile (99.8% anhydrous, Sigma Aldrich, CAS: 75-05-8). The as-prepared solution was then deposited on top of the absorber by spin coating at 4,000 rpm for 30 s in nitrogen atmosphere without any post-annealing. Devices employing spiro-MeOTAD were kept in an oxygen atmosphere at 25% relative humidity overnight. For solar cells in p-i-n architecture, a 25 nm thick C_{60} fullerene layer (Alfa Aesar, 98%, CAS: 99685-96-8) followed by a 3 nm thick bathocuproine (BCP, Luminescence Technology, CAS: 4733-39-5) layer was thermally evaporated in a Spectros evaporation system (Kurt J. Lesker Company) as the electron transport layer on top of the absorber. Finally, an 80 nm thick gold or silver contact was deposited, giving an active device area of 0.105 cm^2.

Characterization: Current-density-voltage characteristics were measured in a solar simulator with a xenon lamp (Newport Oriel Sol3A) under AM1.5G spectra (100 mW cm^{-2}) in both forward and backward direction at a scan speed of 0.6 V s^{-1}. The intensity was calibrated with a silicon reference solar cell equipped with a KG5 band pass filter. During the measurement, the temperature of the solar cells was kept at 25 °C by using a Peltier element controlled by a microcontroller. MPP tracking by using a perturb-and-observe method was performed as well. For XRD investigations, a Bruker D8 DISCOVER system with Cu-K$_\alpha$ radiation was used and measurements were performed in Bragg-Brentano configuration. Scanning electron microscope (SEM) investigations were carried out in a scanning electron microscope (Zeiss LEO1530) with an in-lens detector and an aperture size of 20 µm. For cross-sectional investigations the cross sections were covered with a 3 nm thick platinum layer deposited by sputtering to prevent charging. For both the XRD and SEM investigations, special air-tight sample holders were employed to prevent any contact to air during transfer and measurement of the samples. For the contact angle measurements, a DataPhysics Instruments GmbH optical contact angle and drop contour analyzer OCA 200 was used, equipped with a high-speed camera (frame rate up to 2450 fps) to allow for an accurate measurement before detrimental solvent-surface interactions set in. In order to guarantee similar surface properties as during the evaporation process, substrates not fabricated via vacuum-based methods were kept in vacuum (<5 × 10^{-7} mbar) overnight and measured immediately after removing. Atomic force microscopy (AFM) investigations were performed by using a JPK nanoWizard II atomic force microscope in intermittent contact mode under ambient conditions. EQE measurements were performed in a Bentham PVE300 system using a halogen and xenon lamp. The aperture size of the illumination was 2.25 mm^2 and a chopper frequency in the range of 585 Hz was used. Optical characteristics were extracted out of transmittance and reflectance data, which were measured in the same system. Absorptance was calculated based on the measured reflectance and transmittance by using the formula $A = 1 - R - T$. Both optical measurements were performed in inert atmosphere. The XPS measurements were performed at the DAISY-SOL cluster tool (DArmstadt Integrated SYstem for SOLar Research) in Darmstadt using an Escalab 250 of Thermo Fisher Scientific, equipped with a XR6 monochromatized Aluminum K alpha X-ray source. From their preparation up until the XPS measurements, samples were kept under nitrogen or vacuum at all times. The XPS spectra were acquired using a pass energy of 10 eV and step sizes of 0.05 eV. The number of scans was adjusted depending on the respective element to achieve a reasonable signal to noise ratio. For the calibration, the Fermi edge of silver (0 eV), the Au4f$_{7/2}$ (84.0 eV), the Ag3d$_{5/2}$ (368.26 eV) and the Cu2p$_{3/2}$ (932.69 eV) emission line of sputter cleaned metal surfaces were recorded. Peak fitting was performed in the Avantage software of Thermo Fisher by using a convolution of a Gaussian and a Lorentzian peak after a Shirly background subtraction. In order to determine the elemental ratios, the fitted peak areas were divided by the Scofield sensitivity factors taken from the Avantage software, the machine specific transmission function, and the mean free path.

Supporting Information

Supporting Information is available from the Wiley Online Library or from the author.

Acknowledgements

Conflict of Interest

The authors declare no conflict of interest.

Data Availability Statement

The data that supports the findings of this study are available in the supplementary material of this article.

[1] B. R. Sutherland, E. H. Sargent, *Nat. Photonics* **2016**, *10*, 295.

[2] H. Wei, J. Huang, *Nat. Commun.* **2019**, *10*, 1066.

[3] A. K. Jena, A. Kulkarni, T. Miyasaka, *Chem. Rev.* **2019**, *119*, 3036.

[4] National Renewable Energy Laboratory (NREL), Best Research-Cell Efficiencies, https://www.nrel.gov/pv/cell-efficiency.html (accessed: June 2021).

[5] M. A. Green, E. D. Dunlop, J. Hohl-Ebinger, M. Yoshita, N. Kopidakis, X. Hao, *Prog. Photovoltaics* **2020**, *28*, 629.

[6] S. De Wolf, J. Holovsky, S.-J. Moon, P. Löper, B. Niesen, M. Ledinsky, F.-J. Haug, J.-H. Yum, C. Ballif, *J. Phys. Chem. Lett.* **2014**, *5*, 1035.

[7] S. D. Stranks, G. E. Eperon, G. Grancini, C. Menelaou, M. J. P. Alcocer, T. Leijtens, L. M. Herz, A. Petrozza, H. J. Snaith, *Science* **2013**, *342*, 341.

[8] M. R. Filip, G. E. Eperon, H. J. Snaith, F. Giustino, *Nat. Commun.* **2014**, *5*, 5757.

[9] E. L. Unger, L. Kegelmann, K. Suchan, D. Sörell, L. Korte, S. Albrecht, *J. Mater. Chem. A* **2017**, *5*, 11401.

[10] M. Saliba, J.-P. Correa-Baena, C. M. Wolff, M. Stolterfoht, N. Phung, S. Albrecht, D. Neher, A. Abate, *Chem. Mater.* **2018**, *30*, 4193.

[11] Q. Jiang, Y. Zhao, X. Zhang, X. Yang, Y. Chen, Z. Chu, Q. Ye, X. Li, Z. Yin, J. You, *Nat. Photonics* **2019**, *13*, 460.

[12] M. Jeong, I. W. Choi, E. M. Go, Y. Cho, M. Kim, B. Lee, S. Jeong, Y. Jo, H. W. Choi, J. Lee, J.-H. Bae, S. K. Kwak, D. S. Kim, C. Yang, *Science* **2020**, *369*, 1615.

[13] R. Patidar, D. Burkitt, K. Hooper, D. Richards, T. Watson, *Mater. Today Commun.* **2020**, *22*, 100808.

[14] A. S. Subbiah, F. H. Isikgor, C. T. Howells, M. De Bastiani, J. Liu, E. Aydin, F. Furlan, T. G. Allen, F. Xu, S. Zhumagali, S. Hoogland, E. H. Sargent, I. McCulloch, S. De Wolf, *ACS Energy Lett.* **2020**, *5*, 3034.

[15] Y. Y. Kim, E. Y. Park, T.-Y. Yang, J. H. Noh, T. J. Shin, N. J. Jeon, J. Seo, *J. Mater. Chem. A* **2018**, *6*, 12447.

[16] F. Mathies, E. J. W. List-Kratochvil, E. L. Unger, *Energy Technol.* **2020**, *8*, 1900991.

[17] H. Eggers, F. Schackmar, T. Abzieher, Q. Sun, U. Lemmer, Y. Vaynzof, B. S. Richards, G. Hernandez-Sosa, U. W. Paetzold, *Adv. Energy Mater.* **2020**, *10*, 1903184.

[18] Z. Li, P. Li, G. Chen, Y. Cheng, X. Pi, X. Yu, D. Yang, L. Han, Y. Zhang, Y. Song, *ACS Appl. Mater. Interfaces* **2020**, *12*, 39082.

[19] J. E. Bishop, J. A. Smith, D. G. Lidzey, *ACS Appl. Mater. Interfaces* **2020**, *12*, 48237.

[20] J. E. Bishop, C. D. Read, J. A. Smith, T. J. Routledge, D. G. Lidzey, *Sci. Rep.* **2020**, *10*, 6610.

[21] X. Yu, X. Yan, J. Xiao, Z. Ku, J. Zhong, W. Li, F. Huang, Y. Peng, Y.-B. Cheng, *J. Chem. Phys.* **2020**, *153*, 014706.

[22] Y. Rong, Y. Hu, A. Mei, H. Tan, M. I. Saidaminov, S. I. Seok, M. D. McGehee, E. H. Sargent, H. Han, *Science* **2018**, *361*, eaat8235.

[23] J. Ávila, C. Momblona, P. P. Boix, M. Sessolo, H. J. Bolink, *Joule* **2017**, *1*, 431.

[24] Y. Vaynzof, *Adv. Energy Mater.* **2020**, *10*, 2003073.

[25] D. B. Mitzi, M. T. Prikas, K. Chondroudis, *Chem. Mater.* **1999**, *11*, 542.

[26] A. Kojima, K. Teshima, Y. Shirai, T. Miyasaka, *J. Am. Chem. Soc.* **2009**, *131*, 6050.

[27] M. Liu, M. B. Johnston, H. J. Snaith, *Nature* **2013**, *501*, 395ö.

[28] J. Teuscher, A. Ulianov, O. Müntener, M. Grätzel, N. Tétreault, *ChemSusChem* **2015**, *8*, 3847.

[29] B. S. Kim, M. H. Choi, M. S. Choi, J. J. Kim, *J. Mater. Chem. A* **2016**, *4*, 5663.

[30] S. Y. Hsiao, H. L. Lin, W. H. Lee, W. L. Tsai, K. M. Chiang, W. Y. Liao, C. Z. Ren-Wu, C. Y. Chen, H. W. Lin, *Adv. Mater.* **2016**, *28*, 7013.

[31] M. M. Tavakoli, A. Simchi, X. Mo, Z. Fan, *Mater. Chem. Front.* **2017**, *1*, 1520.

[32] M. M. Tavakoli, P. Yadav, D. Prochowicz, R. Tavakoli, M. Saliba, *J. Phys. D: Appl. Phys.* **2018**, *52*, 034005.

[33] J. A. Raiford, S. T. Oyakhire, S. F. Bent, *Energy Environ. Sci.* **2020**, *13*, 1997.

[34] C. Momblona, L. Gil-Escrig, E. Bandiello, E. M. Hutter, M. Sessolo, K. Lederer, J. Blochwitz-Nimoth, H. J. Bolink, *Energy Environ. Sci.* **2016**, *9*, 3456.

[35] W. Ke, D. Zhao, C. R. Grice, A. J. Cimaroli, G. Fang, Y. Yan, *J. Mater. Chem. A* **2015**, *3*, 23888.

[36] B.-S. Kim, T.-M. Kim, M.-C. Choi, H.-S. Shim, J.-J. Kim, *Org. Electron.* **2015**, *17*, 102.

[37] T. Abzieher, S. Moghadamzadeh, F. Schackmar, H. Eggers, F. Sutterlüti, A. Farooq, D. Kojda, K. Habicht, R. Schmager, A. Mertens, R. Azmi, L. Klohr, J. A. Schwenzer, M. Hetterich, U. Lemmer, B. S. Richards, M. Powalla, U. W. Paetzold, *Adv. Energy Mater.* **2019**, *9*, 1802995.

[38] T. Abzieher, J. A. Schwenzer, S. Moghadamzadeh, F. Sutterlüti, I. M. Hossain, M. Pfau, E. Lotter, M. Hetterich, B. S. Richards, U. Lemmer, M. Powalla, U. W. Paetzold, *IEEE J. Photovoltaics* **2019**, *9*, 1249.

[39] M. M. Tavakoli, P. Yadav, D. Prochowicz, R. Tavakoli, *Sol. RRL* **2021**, *5*, 2000552.

[40] D. Pérez-del-Rey, P. P. Boix, M. Sessolo, A. Hadipour, H. J. Bolink, *J. Phys. Chem. Lett.* **2018**, *9*, 1041.

[41] M. M. Tavakoli, R. Tavakoli, *Phys. Status Solidi RRL* **2021**, *15*, 2000449.

[42] L. Gil-Escrig, C. Momblona, M. G. La-Placa, P. P. Boix, M. Sessolo, H. J. Bolink, *Adv. Energy Mater.* **2018**, *8*, 1703506.

[43] R. Kottokkaran, H. A. Gaonkar, B. Bagheri, V. L. Dalal, *J. Vac. Sci. Technol., A* **2018**, *36*, 041201.

[44] C.-G. Park, W.-G. Choi, S. Na, T. Moon, *Electron. Mater. Lett.* **2019**, *15*, 56.

[45] R. Ji, Z. Zhang, C. Cho, Q. An, F. Paulus, M. Kroll, M. Löffler, F. Nehm, B. Rellinghaus, K. Leo, Y. Vaynzof, *J. Mater. Chem. C* **2020**, *8*, 7725.

[46] Y.-H. Chiang, M. Anaya, S. D. Stranks, *ACS Energy Lett.* **2020**, *5*, 2498.

[47] Y. Yu, D. Zhao, C. R. Grice, W. Meng, C. Wang, W. Liao, A. J. Cimaroli, H. Zhang, K. Zhu, Y. Yan, *RSC Adv.* **2016**, *6*, 90248.

[48] P. Fan, H.-X. Peng, Z.-H. Zheng, Z.-H. Chen, S.-J. Tan, X.-Y. Chen, Y.-D. Luo, Z.-H. Su, J.-T. Luo, G.-X. Liang, *Nanomaterials* **2019**, *9*, 1760.

[49] J. M. Ball, L. Buizza, H. C. Sansom, M. D. Farrar, M. T. Klug, J. Borchert, J. Patel, L. M. Herz, M. B. Johnston, H. J. Snaith, *ACS Energy Lett.* **2019**, *4*, 2748.

[50] M. Saliba, T. Matsui, J.-Y. Seo, K. Domanski, J.-P. Correa-Baena, M. K. Nazeeruddin, S. M. Zakeeruddin, W. Tress, A. Abate, A. Hagfeldt, M. Grätzel, *Energy Environ. Sci.* **2016**, *9*, 1989.

[51] W. Rehman, D. P. McMeekin, J. B. Patel, R. L. Milot, M. B. Johnston, H. J. Snaith, L. M. Herz, *Energy Environ. Sci.* **2017**, *10*, 361.

[52] M. Jošt, L. Kegelmann, L. Korte, S. Albrecht, *Adv. Energy Mater.* **2020**, *10*, 1904102.

**ADVANCED
SCIENCE NEWS**

www.advancedsciencenews.com

**ADVANCED
FUNCTIONAL
MATERIALS**

www.afm-journal.de

[53] G. E. Eperon, T. Leijtens, K. A. Bush, R. Prasanna, T. Green, J. T.-W. Wang, D. P. McMeekin, G. Volonakis, R. L. Milot, R. May, A. Palmstrom, D. J. Slotcavage, R. A. Belisle, J. B. Patel, E. S. Parrott, R. J. Sutton, W. Ma, F. Moghadam, B. Conings, A. Babayigit, H.-G. Boyen, S. Bent, F. Giustino, L. M. Herz, M. B. Johnston, M. D. McGehee, H. J. Snaith, *Science* **2016**, *354*, 861.

[54] R. Lin, K. Xiao, Z. Qin, Q. Han, C. Zhang, M. Wei, M. I. Saidaminov, Y. Gao, J. Xu, M. Xiao, A. Li, J. Zhu, E. H. Sargent, H. Tan, *Nat. Energy* **2019**, *4*, 864.

[55] Z. Yu, Z. Yang, Z. Ni, Y. Shao, B. Chen, Y. Lin, H. Wei, Z. J. Yu, Z. Holman, J. Huang, *Nat. Energy* **2020**, *5*, 657.

[56] K. A. Bush, A. F. Palmstrom, Z. J. Yu, M. Boccard, R. Cheacharoen, J. P. Mailoa, D. P. McMeekin, R. L. Z. Hoye, C. D. Bailie, T. Leijtens, I. M. Peters, M. C. Minichetti, N. Rolston, R. Prasanna, S. Sofia, D. Harwood, W. Ma, F. Moghadam, H. J. Snaith, T. Buonassisi, Z. C. Holman, S. F. Bent, M. D. McGehee, *Nat. Energy* **2017**, *2*, 17009.

[57] B. Chen, Z. Yu, K. Liu, X. Zheng, Y. Liu, J. Shi, D. Spronk, P. N. Rudd, Z. Holman, J. Huang, *Joule* **2019**, *3*, 177.

[58] F. Sahli, J. Werner, A. K. Brett, M. Bräuninger, R. Monnard, B. Paviet-Salomon, L. Barraud, L. Ding, J. J. D. Leon, D. Sacchetto, G. Cattaneo, M. Despeisse, M. Boccard, S. Nicolay, Q. Jeangros, B. Niesen, C. Ballif, *Nat. Mater.* **2018**, *17*, 820.

[59] Q. Han, Y.-T. Hsieh, L. Meng, J.-L. Wu, P. Sun, E.-P. Yao, S.-Y. Chang, S.-H. Bae, T. Kato, V. Bermudez, Y. Yang, *Science* **2018**, *361*, 904.

[60] A. Al-Ashouri, A. Magomedov, M. Roß, M. Jošt, M. Talaikis, G. Chistiakova, T. Bertram, J. A. Márquez, E. Köhnen, E. Kasparavičius, S. Levcenco, L. Gil-Escrig, C. J. Hages, R. Schlatmann, B. Rech, T. Malinauskas, T. Unold, C. A. Kaufmann, L. Korte, G. Niaura, V. Getautis, S. Albrecht, *Energy Environ. Sci.* **2019**, *12*, 3356.

[61] G. Longo, C. Momblona, M. G. La-Placa, L. Gil-Escrig, M. Sessolo, H. J. Bolink, *ACS Energy Lett.* **2018**, *3*, 214.

[62] L. Cojocaru, K. Wienands, T. W. Kim, S. Uchida, A. J. Bett, S. Rafizadeh, J. C. Goldschmidt, S. W. Glunz, *ACS Appl. Mater. Interfaces* **2018**, *10*, 26293.

[63] K. Hamada, K. Yonezawa, K. Yamamoto, T. Taima, S. Hayase, N. Ooyagi, Y. Yamamoto, K. Ohdaira, *Jpn. J. Appl. Phys.* **2019**, *58*, SBBF06.

[64] L. Gil-Escrig, M. Roß, J. Sutter, A. Al-Ashouri, C. Becker, S. Albrecht, *Sol. RRL* **2021**, *5*, 2000553.

[65] H. Xu, Y. Wu, J. Cui, C. Ni, F. Xu, J. Cai, F. Hong, Z. Fang, W. Wang, J. Zhu, L. Wang, R. Xu, F. Xu, *Phys. Chem. Chem. Phys.* **2016**, *18*, 18607.

[66] S. Olthof, K. Meerholz, *Sci. Rep.* **2017**, *7*, 40267.

[67] R. C. Shallcross, S. Olthof, K. Meerholz, N. R. Armstrong, *ACS Appl. Mater. Interfaces* **2019**, *11*, 32500.

[68] J. B. Patel, J. Wong-Leung, S. Van Reenen, N. Sakai, J. T. W. Wang, E. S. Parrott, M. Liu, H. J. Snaith, L. M. Herz, M. B. Johnston, *Adv. Electron. Mater.* **2017**, *3*, 1600470.

[69] E. S. Parrott, J. B. Patel, A. A. Haghighirad, H. J. Snaith, M. B. Johnston, L. M. Herz, *Nanoscale* **2019**, *11*, 14276.

[70] P. Pistor, J. Borchert, W. Fränzel, R. Csuk, R. Scheer, *J. Phys. Chem. Lett.* **2014**, *5*, 3308.

[71] J. Li, H. Wang, X. Y. Chin, H. A. Dewi, K. Vergeer, T. W. Goh, J. W. M. Lim, J. H. Lew, K. P. Loh, C. Soci, T. C. Sum, H. J. Bolink, N. Mathews, S. Mhaisalkar, A. Bruno, *Joule* **2020**, *4*, 1035.

[72] O. Malinkiewicz, C. Roldán-Carmona, A. Soriano, E. Bandiello, L. Camacho, M. K. Nazeeruddin, H. J. Bolink, *Adv. Energy Mater.* **2014**, *4*, 1400345.

[73] O. Malinkiewicz, A. Yella, Y. H. Lee, G. M. Espallargas, M. Graetzel, M. K. Nazeeruddin, H. J. Bolink, *Nat. Photonics* **2014**, *8*, 128.

[74] J. C. S. Costa, J. Azevedo, L. M. N. B. F. Santos, A. Mendes, *J. Phys. Chem. C* **2017**, *121*, 2080.

[75] B. S. Kim, L. Gil-Escrig, M. Sessolo, H. J. Bolink, *J. Phys. Chem. Lett.* **2020**, *11*, 6852.

[76] J. C. S. Costa, J. Azevedo, J. P. Araújo, L. M. N. B. F. Santos, A. Mendes, *Thin Solid Films* **2018**, *664*, 12.

[77] R. D. Shannon, *Acta Crystallogr.* **1976**, *A32*, 751.

[78] G. Kieslich, S. Sun, A. K. Cheetham, *Chem. Sci.* **2014**, *5*, 4712.

[79] M. J. Bækbo, O. Hansen, I. Chorkendorff, P. C. K. Vesborg, *RSC Adv.* **2018**, *8*, 29899.

[80] T. J. Jacobsson, J. P. Correa-Baena, E. H. Anaraki, B. Philippe, S. D. Stranks, M. E. F. Bouduban, W. Tress, K. Schenk, J. Teuscher, J. E. Moser, H. Rensmo, A. Hagfeldt, *J. Am. Chem. Soc.* **2016**, *138*, 10331.

[81] K. M. Boopathi, R. Mohan, T. Y. Huang, W. Budiawan, M. Y. Lin, C. H. Lee, K. C. Ho, C. W. Chu, *J. Mater. Chem. A* **2016**, *4*, 1591.

[82] M. Becker, M. Wark, Z. Naturforsch, *A: Phys. Sci.* **2019**, *74*, 655.

[83] N. Pant, A. Kulkarni, M. Yanagida, Y. Shirai, T. Miyasaka, K. Miyano, *ACS Appl. Energy Mater.* **2020**, *3*, 6215.

[84] W. Nie, H. Tsai, R. Asadpour, J.-C. Blancon, A. J. Neukirch, G. Gupta, J. J. Crochet, M. Chhowalla, S. Tretiak, M. A. Alam, H.-L. Wang, A. D. Mohite, *Science* **2015**, *347*, 522.

[85] L. Han, S. Cong, H. Yang, Y. Lou, H. Wang, J. Huang, J. Zhu, Y. Wu, Q. Chen, B. Zhang, L. Zhang, G. Zou, *Sol. RRL* **2018**, *2*, 1800054.

[86] K. Liao, J.-A. Yang, C. Li, T. Li, F. Hao, *ACS Appl. Mater. Interfaces* **2019**, *11*, 39882.

[87] J. V. Patil, S. S. Mali, C. K. Hong, *Nanoscale* **2019**, *11*, 21824.

[88] F. Palazon, Y. El Ajjouri, H. J. Bolink, *Adv. Energy Mater.* **2020**, *10*, 1902499.

[89] J. A. Marqusee, J. Ross, *J. Chem. Phys.* **1983**, *79*, 373.

[90] F. Mathies, H. Eggers, B. S. Richards, G. Hernandez-Sosa, U. Lemmer, U. W. Paetzold, *ACS Appl. Energy Mater.* **2018**, *1*, 1834.

[91] Y.-C. Chern, Y.-C. Chen, H.-R. Wu, H.-W. Zan, H.-F. Meng, S.-F. Horng, *Org. Electron.* **2016**, *38*, 362.

[92] H. Do Kim, H. Ohkita, H. Benten, S. Ito, *Adv. Mater.* **2016**, *28*, 917.

[93] B. Lee, T. Hwang, S. Lee, B. Shin, B. Park, *Sci. Rep.* **2019**, *9*, 4803.

[94] A. F. Castro-Méndez, J. Hidalgo, J. P. Correa-Baena, *Adv. Energy Mater.* **2019**, *9*, 1901489.

[95] G. Madras, B. J. McCoy, *J. Chem. Phys.* **2003**, *119*, 1683.

[96] G. Madras, B. J. McCoy, *Chem. Eng. Sci.* **2004**, *59*, 2753.

[97] T. Leijtens, G. E. Eperon, S. Pathak, A. Abate, M. M. Lee, H. J. Snaith, *Nat. Commun.* **2013**, *4*, 2885.

[98] A. Farooq, I. M. Hossain, S. Moghadamzadeh, J. A. Schwenzer, T. Abzieher, B. S. Richards, E. Klampaftis, U. W. Paetzold, *ACS Appl. Mater. Interfaces* **2018**, *10*, 21985.

[99] C. C. Boyd, R. C. Shallcross, T. Moot, R. Kerner, L. Bertoluzzi, A. Onno, S. Kavadiya, C. Chosy, E. J. Wolf, J. Werner, J. A. Raiford, C. de Paula, A. F. Palmstrom, Z. J. Yu, J. J. Berry, S. F. Bent, Z. C. Holman, J. M. Luther, E. L. Ratcliff, N. R. Armstrong, M. D. McGehee, *Joule* **2020**, *4*, 1759.

[100] K. Schutt, P. K. Nayak, A. J. Ramadan, B. Wenger, Y. H. Lin, H. J. Snaith, *Adv. Funct. Mater.* **2019**, *29*, 1900466.

[101] C. Bi, Q. Wang, Y. Shao, Y. Yuan, Z. Xiao, J. Huang, *Nat. Commun.* **2015**, *6*, 7747.

[102] M. Schultes, N. Giesbrecht, J. Küffner, E. Ahlswede, P. Docampo, T. Bein, M. Powalla, *ACS Appl. Mater. Interfaces* **2019**, *11*, 12948.

[103] F. Guo, S. Qiu, J. Hu, H. Wang, B. Cai, J. Li, X. Yuan, X. Liu, K. Forberich, C. J. Brabec, Y. Mai, *Adv. Sci.* **2019**, *6*, 1901067.

[104] L. Zeng, S. Chen, K. Forberich, C. J. Brabec, Y. Mai, F. Guo, *Energy Environ. Sci.* **2020**, *13*, 4666.

[105] C. Momblona, O. Malinkiewicz, C. Roldán-Carmona, A. Soriano, L. Gil-Escrig, E. Bandiello, M. Scheepers, E. Edri, H. J. Bolink, *APL Mater.* **2014**, *2*, 081504.

[106] A. Al-Ashouri, E. Köhnen, B. Li, A. Magomedov, H. Hempel, P. Caprioglio, J. A. Márquez, A. B. Morales Vilches, E. Kasparavicius, J. A. Smith, N. Phung, D. Menzel, M. Grischek, L. Kegelmann, D. Skroblin, C. Gollwitzer, T. Malinauskas, M. Jošt, G. Matič, B. Rech, R. Schlatmann, M. Topič, L. Korte, A. Abate,

**ADVANCED
SCIENCE NEWS**

www.advancedsciencenews.com

**ADVANCED
FUNCTIONAL
MATERIALS**

www.afm-journal.de

B. Stannowski, D. Neher, M. Stolterfoht, T. Unold, V. Getautis, S. Albrecht, *Science* **2020**, *370*, 1300.

[107] M. Roß, L. Gil-Escrig, A. Al-Ashouri, P. Tockhorn, M. Jošt, B. Rech, S. Albrecht, *ACS Appl. Mater. Interfaces* **2020**, *12*, 39261.

[108] Q. Chen, H. Zhou, T.-B. Song, S. Luo, Z. Hong, H.-S. Duan, L. Dou, Y. Liu, Y. Yang, *Nano Lett.* **2014**, *14*, 4158.

[109] L. Wang, C. McCleese, A. Kovalsky, Y. Zhao, C. Burda, *J. Am. Chem. Soc.* **2014**, *136*, 12205.

[110] B.-W. Park, N. Kedem, M. Kulbak, D. Y. Lee, W. S. Yang, N. J. Jeon, J. Seo, G. Kim, K. J. Kim, T. J. Shin, G. Hodes, D. Cahen, S. Il Seok, *Nat. Commun.* **2018**, *9*, 3301.

[111] I. M. Hossain, D. Hudry, F. Mathies, T. Abzieher, S. Moghadamzadeh, D. Rueda-Delgado, F. Schackmar, M. Bruns, R. Andriessen, T. Aernouts, F. Di Giacomo, U. Lemmer, B. S. Richards, U. W. Paetzold, A. Hadipour, *ACS Appl. Energy Mater.* **2019**, *2*, 47.

[112] S. Moghadamzadeh, I. M. Hossain, M. Jakoby, B. Abdollahi Nejand, D. Rueda-Delgado, J. A. Schwenzer, S. Gharibzadeh, T. Abzieher, M. R. Khan, A. A. Haghighirad, I. A. Howard,

B. S. Richards, U. Lemmer, U. W. Paetzold, *J. Mater. Chem. A* **2020**, *8*, 670.

[113] R. Schmager, J. Roger, J. A. Schwenzer, F. Schackmar, T. Abzieher, M. Malekshahi Byranvand, B. Abdollahi Nejand, M. Worgull, B. S. Richards, U. W. Paetzold, *Adv. Funct. Mater.* **2020**, *30*, 1907481.

[114] L. E. Polander, P. Pahner, M. Schwarze, M. Saalfrank, C. Koerner, K. Leo, *APL Mater.* **2014**, *2*, 081503.

[115] G. Nogay, F. Sahli, J. Werner, R. Monnard, M. Boccard, M. Despeisse, F. J. Haug, Q. Jeangros, A. Ingenito, C. Ballif, *ACS Energy Lett.* **2019**, *4*, 844.

[116] R. Swartwout, M. T. Hoerantner, V. Bulović, *Energy Environ. Mater.* **2019**, *2*, 119.

[117] H. D. Pham, L. Gil-Escrig, K. Feron, S. Manzhos, S. Albrecht, H. J. Bolink, P. Sonar, *J. Mater. Chem. A* **2019**, *7*, 12507.

[118] J. Li, H. A. Dewi, H. Wang, J. H. Lew, N. Mathews, S. Mhaisalkar, A. Bruno, *Sol. RRL* **2020**, *4*, 2000473.

[119] PV-Magazine, Large-Area Perovskite Solar Module with 18% Efficiency, https://www.pv-magazine.com/2021/04/28/large-area-perovskite-solar-module-with-18-efficiency/ (accessed: June 2021).

2104482 (19 of 19)